

Photoionization Studies of Reactive Intermediates

using Synchrotron Radiation

by

John M.Dyke*

School of Chemistry
University of Southampton
SO17 1BJ
UK

*e-mail: jmdyke@soton.ac.uk

Abstract

Photoionization of reactive intermediates with synchrotron radiation has reached a sufficiently advanced stage of development that it can now contribute to a number of areas in gas-phase chemistry and physics. These include the detection and spectroscopic study of reactive intermediates produced by bimolecular reactions, photolysis, pyrolysis or discharge sources, and the monitoring of reactive intermediates *in situ* in environments such as flames.

This review summarises advances in the study of reactive intermediates with synchrotron radiation using photoelectron spectroscopy (PES) and constant-ionic-state (CIS) methods with angular resolution, and threshold photoelectron spectroscopy (TPES), taking examples mainly from the recent work of the Southampton group. The aim is to focus on the main information to be obtained from the examples considered.

As future research in this area also involves photoelectron-photoion coincidence (PEPICO) and threshold photoelectron-photoion coincidence (TPEPICO) spectroscopy, these methods are also described and previous related work on reactive intermediates with these techniques is summarised. The advantages of using PEPICO and TPEPICO to complement and extend TPES and angularly resolved PES and CIS studies on reactive intermediates are highlighted.

1.Introduction

This review is organised as follows. After an Introduction to the study of reactive intermediates by photoionization with fixed energy photon sources and synchrotron radiation, a number of Case Studies are presented of the study of reactive intermediates with synchrotron radiation using angle resolved PES and CIS, and TPE spectroscopy. Then directions of Future Research in this field, which include use of PEPICO and TPEPICO spectroscopy, are considered.

1.1 Use of photoionization to study reactive intermediates

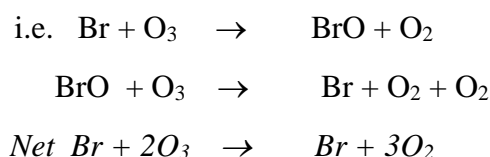
Reactive intermediates are found in all areas of chemistry (1). Although they are often present in low concentrations and may have short lifetimes, they can play key roles in determining reaction products and the branching ratios between different product channels. This arises because a reactive intermediate often represents a branching point on a reaction surface with paths leading to two or more sets of products. Understanding the ratio of the products from different channels necessitates understanding the properties of the reactive intermediate as well as the details of the potential energy surface. A reaction potential energy surface will in general contain a number of minima and maxima. The minima are the reactants, a reaction complex (RC), a product complex (PC) and the products. A transition state (TS), a maximum on the surface, will lie between the PC and the RC. If a reaction proceeds via a reactive intermediate, this will be an extra minimum on the surface which lies between the RC and the PC. The RC, reactive intermediate and PC will then be separated by transition states (TS1 and TS2), and the overall reaction can then be written as

$$\text{reactants} \rightarrow \text{RC} \rightarrow \text{TS1} \rightarrow \text{reactive intermediate} \rightarrow \text{TS2} \rightarrow \text{PC} \rightarrow \text{products}.$$

An example of a reaction that proceeds via a reaction intermediate is the atmospherically important reaction $\text{Cl}_2 + \text{CH}_3\text{SCH}_3$. This proceeds via the covalently bound intermediate $\text{Cl}_2\text{S}(\text{CH}_3)_2$ before forming the final products $\text{CH}_3\text{SCH}_2 + \text{HCl}$. Photoelectron spectroscopy (PES) and electronic structure calculations have been used to investigate the structure and bonding of this reactive intermediate and obtain information on the reaction surface (2). Also, the room temperature rate coefficient of the $\text{Cl}_2 + \text{CH}_3\text{SCH}_3$ reaction has been measured using PES as the detection method (3).

Reactive intermediates play key roles in environments such as flames, plasmas, and the earth's atmosphere. Their concentrations are invariably low because they are typically produced by one reaction and removed by another reaction, and as a result, their concentrations are determined by the initial concentrations of the reactants and the rate

coefficients of the two consecutive reactions. An example is the BrO radical prepared from the Br + O₃ reaction. In a multiple collision environment Br + O₃ produces BrO and then BrO is removed by reaction with O₃, as shown in the consecutive reactions below:-



By studying the Br + O₃ reaction at short reaction times, using efficient pumping and electron detection methods, it proved possible to obtain sufficient concentrations of BrO to use PES to study its electronic structure and determine ionization energies to its low-lying ionic states. Also from the vibrationally resolved photoelectron bands, spectroscopic constants (equilibrium bond lengths, r_e , and vibrational constants ω_e and $\omega_e x_e$) were obtained for the ionic states (4).

The detection of the electrons or the ions produced in photoionization is an excellent way of monitoring reactive intermediates and products from different reaction channels to measure product branching ratios. Two methods are often used, PES and photoionization mass spectrometry (PIMS), depending on whether electrons or ions are detected. In PES (5) the electron energy distribution is measured at fixed photon energy. This gives information on the electronic and geometric structure of the molecular species ionized. In PIMS (6) ion intensities are measured at fixed photon energy. If too high a photon energy is used, fragmentation of the parent ion will occur with the ions observed being fragments of the parent ion. However, if the parent ion is observed, its intensity can be monitored as a function of photon energy to obtain an ionization efficiency curve. This can then be used to estimate the associated adiabatic ionization energy (AIE, the difference between the lowest vibrational levels of the molecule and its cation in their ground electronic states) by measuring the parent ion intensity at photon energies just above the ionization energy and extrapolating the ionization efficiency curve back to the onset of ionization. In the absence of fragmentation, and effects arising from autoionization resonances, the photoionization efficiency (PIE) curve for a selected neutral molecule is essentially the integral of its photoelectron spectrum. (In a vibrationally resolved PE band, the vertical ionization energy, VIE, is the most intense component and the AIE is the first component).

Photoionization processes of reactive intermediates are of fundamental importance, and find application in a large number of scientific areas, including astrophysics, planetary science, the chemistry of the earth's atmosphere, radiation chemistry, physics and biology.

Researchers in these fields require ionization energies, fragment appearance energies, and information on electronic excited neutral states and low-lying ionic states, as well as measures of intensities (relative and absolute cross-sections) for photoabsorption, photoionization, and photofragmentation processes over a wide spectral range. PES and PIMS measurements on reactive intermediates, supported by electronic structure calculations, help to understand their structure and reactivity in environments such as plasmas, flames, the earth's atmosphere and in solution. Also, measurements of ionization energies of reactive intermediates lead to determination of key thermochemical quantities such as heats of formation and bond dissociation energies, which are valuable in calculations relevant to these environments (7,8).

For example, the first AIE of a molecular reactive intermediate is equal to the difference in the heats of formation of the cation and the neutral molecule. If the heat of formation of the cation is available from other sources, for example from proton affinity studies, then the heat of formation of the neutral molecule can be obtained. If a stable molecule ABC is considered with reactive fragments AB and C, which are usually fragments with unpaired electrons (free radicals), then the following ionization processes are possible:-



If the AIEs of ABC and AB can be measured for processes (1) and (3), and the appearance energy (AE) of AB^+ can be measured for step (2), then from the AE of AB^+ and the AIE of ABC, the dissociation energy of AB^+-C , $D(AB^+-C)$, can be calculated, using equation (4):-

$$D(AB^+-C) = AE(AB^+) - AIE(ABC) \quad \text{-----(4)}$$

Also, from the $AE(AB^+)$ in equation (2) and the AIE of AB in equation (3), the neutral dissociation energy $D(AB-C)$ can be calculated

$$D(AB-C) = AE(AB^+) - AIE(AB) \quad \text{-----(5)}$$

Thermodynamic cycle calculations of this type have been used extensively to determine heats of formation of reactive intermediates and bond strengths in molecules and ions (9-11). This information is important in modelling the atmosphere and other environments, and in benchmarking theoretical methods used to calculate these quantities.

For example, modelling of ozone in the stratosphere requires its ionization energy and electron affinity, and also modelling the role of ozone in the lower ionosphere requires knowledge of its direct and dissociative ionization by photons and electrons. The first AIE of ozone was not unambiguously determined until 2005 (12). Prior to that, in PES studies, a weak vibrational component was observed at (12.44 ± 0.01) eV, on the low IE side of the first band, which was assigned to ionization to the vibronic ground state of the cation (13,14). This weak band was not observed in other PES work (15,16), which reported a value of 12.52 eV in agreement with the result of (12.519 ± 0.004) eV obtained by PIMS (17). Also, a value near 12.52 eV had also been suggested on the basis of an analysis of relevant thermochemical cycles (18,19). In more recent work, this discrepancy was resolved in a pulsed-field-ionization zero-kinetic-energy (PFI-ZEKE) photoelectron study of jet-cooled ozone (12) which gave a value for the first adiabatic IE of ozone as (12.52495 ± 0.00006) eV, indicating that the earlier value of (12.44 ± 0.01) eV arises from ionization of vibrationally excited ozone. This highly precise value of the AIE allowed determination of a more accurate value for the lowest dissociation threshold of O_3^+ , $\text{D}(\text{O}_2^+--\text{O})$ as (4898 ± 3) cm^{-1} .

When considering equations (1) to (3) it is important to emphasize, however, that obtaining reliable AEs experimentally is more challenging than obtaining reliable AIEs. The determination of the AIE from a vibrationally resolved PE band is usually reasonably straightforward, particularly if the vibrational envelope can be computed, using potential energy surfaces of the molecule and the ion derived from electronic structure calculations, and there is only a small change in equilibrium geometry between the molecule and the ion. However, to obtain reliable AEs is more difficult. This is because 0 K values are needed to calculate bond dissociation energies (equations 4 and 5) and the internal thermal energy of ABC, possible barriers to dissociation in ABC^+ and slow dissociation of ABC^+ in the vicinity of the dissociation threshold, which gives rise to a so called “kinetic shift”, need to be taken into account in order that experimental breakdown diagrams, the intensities of ABC^+ and AB^+ as a function of photon energy, can be used to obtain 0 K $\text{AE}(\text{AB}^+)$ values (20). Methods have, however, been developed to model and analyse such data (21) to enable reliable $\text{AE}(\text{AB}^+)$ values to be determined.

1.2 Use of photoionization with synchrotron radiation to study reactive intermediates

The study of reactive intermediates with PES using vacuum ultraviolet (vuv) radiation from an inert gas low-pressure discharge photon source is now an established method (7-10). However, using monochromatized synchrotron radiation as the photon source in PES studies allows more information to be obtained on molecular ionic states and the associated photoionization processes than a PES study with a constant energy vuv photon source. In particular

- (i) because the synchrotron photon source is tunable it is possible to identify autoionization resonances, and, once identified, a photoelectron band recorded with photons at these resonance energies can have added intensity in the adiabatic region and extra vibrational structure at higher energy compared to that observed in a PE spectrum recorded off resonance,
- (ii) because the photon source is polarized, angularly resolved photoelectron measurements are possible and this allows information on photoionization dynamics to be obtained,
- (iii) a study of the relative band intensities in the valence PE spectrum of an atom or molecule as a function of photon energy can provide valuable information to assist in band assignment, and
- (iv) by sweeping the photon energy and detecting near-zero kinetic energy electrons, threshold photoelectron (TPE) spectra can be obtained. These are higher resolution than conventional PE spectra and hence may provide more information on the ionization process and the ionic states accessed. A TPE spectrometer has the valuable properties of constant resolution and high collection efficiency (4π steradians collection).

The observation of autoionization in PE spectroscopy, ((i) above), was first observed by Price in 1968 (5,22) when, by recording the NeI and HeI PE spectra of molecular oxygen, it was found that the NeI spectra showed extra vibrational structure arising from autoionization. Also, in PIMS, if autoionization is observed in a PIE curve, information on neutral excited states (Rydberg and inner valence states) can be gained from these autoionization features which, apart from being of fundamental interest, can provide a detailed fingerprint for use in later detection.

It was this feature that initially attracted the Southampton group to use synchrotron radiation because in a number of previous investigations some of the valence PE bands of the reactive intermediate studied, when recorded with a inert gas discharge source, showed an intense adiabatic component with very little intensity in other vibrational components. This is the case for reactive intermediates such as OH, SH, N₃, and CH₃O (9). Such an observation

for the first PE band of a reactive intermediate is particularly disappointing, since measurement of the vibrational level separations in the ground ionic state is usually one of the main experimental objectives. Also, the intensity of a PE band from a reactive intermediate, recorded at a non-resonant photon energy, may be very low and the PE band recorded at a photon energy corresponding to an autoionization resonance should have increased intensity.

This can be seen from Figure 1, which shows schematically the photoelectron vibrational envelope expected for ionization using a photon energy which gives resonant ionization. In this case, the photon energy used matches the energy separation from the ground neutral state (AB) to a neutral excited state (AB*) which is above the ground state of the ion AB⁺. (AB* is a highly excited valence state, or a Rydberg state which is part of a series which converges to an excited state of AB⁺ that has a different equilibrium geometry and vibrational constants from the AB⁺ ground state). On resonant excitation, the neutral excited state (AB*) autoionizes to the lower AB⁺ state. The photoelectron vibrational envelope expected for ionization using a photon energy which gives non-resonant ionization is shown in the Supplementary Information (Figure SI1). In these examples, the potential surfaces of the neutral (AB) and ionic (AB⁺) ground states have been chosen to have the same (or very similar) equilibrium geometrical parameters and vibrational frequencies, and hence only an intense adiabatic component would be expected in the first photoelectron band recorded at a non-resonant photon energy with very little intensity in higher vibrational components (see Figure SI1). This could be viewed as the “worst case scenario”. This arises because the overlap integral of the vibrational wavefunction of the lowest vibrational level of AB, $v''=0$ with the vibrational wavefunction of the lowest vibrational level of AB⁺, $v^+=0$ is close to 1.0, whereas the overlap integrals of the vibrational wavefunction for AB, $v''=0$ with the vibrational wavefunctions of the higher vibrational levels of AB⁺, $v^+ > 0$ are much smaller. The relative intensities of vibrational components in a PE band are governed by the square of the modulus of these overlap integrals (the Franck-Condon factors). In the case of ionization via a resonant state (autoionization), the overlap integrals of the resonant vibrational level v^* of AB* with higher vibrational levels ($v^+ > 0$) of AB⁺ are significant and extra vibrational structure is observed in the PE spectrum. The relative vibrational intensities in the PE envelope obtained by autoionization are determined by the Franck-Condon factors between the resonant excited state (AB*, v^*) and the ion (AB⁺, v^+). If the ionic state, AB⁺, has not been well characterised in previous spectroscopic studies, the improvement in the

values of the vibrational spectroscopic constants of AB^+ from the PE spectrum consisting of resonant and non-resonant parts, compared to those derived from a non-resonant PE spectrum, could be important. Even if the spectroscopic constants of the ionic state are well established, the values of these constants derived from the extended envelope will provide a useful confirmation of the identity of the molecule under investigation. This is particularly relevant for the study of a reaction which proceeds via a reaction intermediate. It is important also to note that in Figure 1, an example of electronic autoionization, there will be an increase in the overall photoelectron signal and hence the overall cross-section on resonant ionization. This is particularly important for the study of reactive intermediates which are invariably present in low concentrations.

Figure 1

A PE spectrometer, which uses a hemispherical electron energy analyser, has been built in the Southampton group to study reactive intermediates with synchrotron radiation (23-25). Three types of spectra can be recorded with this instrument:-

- (a) angularly resolved PE spectra;
- (b) angularly resolved constant-ionic-state (CIS) spectra, and
- (c) threshold photoelectron spectra (TPE) spectra.

A CIS spectrum is obtained by monitoring the intensity of a selected ionic vibrational component AB^+, v^+ as a function of photon energy. The resolution in a CIS spectrum is controlled by the bandwidth of the ionizing radiation used. Relative vibrational intensities in a CIS spectrum for a particular AB^+, v^+ vibrational level can be calculated by multiplying computed Franck-Condon factors for the first ($AB^*, v^* \leftarrow AB, v''=0 + h\nu$) and the second ($AB^+, v^+ + e^- \leftarrow AB^*, v^*$) steps together. The simulated AB^+, v^+ CIS spectrum can then be obtained by plotting the product of Franck-Condon factors against v^* .

In angle resolved PE and CIS measurements, in which the angular distribution parameter (β) is measured as a function of photon energy, the photoionization dynamics of reactive intermediates can be probed. These measurements can determine the angular momentum of the free electron and the phase difference between the continuum waves of the outgoing electron. This gives valuable information about the angular momentum transferred between the initial state (the target) and the final state (the ion and the photoelectron). Also, angular distribution measurements of the β -parameter of vibrational components of a

molecular photoelectron band recorded as a function of photon energy have shown that the β -parameter can change significantly at molecular resonances. This is useful to separate the non-resonant and resonant contributions to the vibrational envelope, and investigate fundamental issues such as the applicability of the Born-Oppenheimer approximation in autoionization from molecular resonances.

Table 1

Many reactive intermediates have unpaired electrons and are therefore classed as open-shell. Studying open-shell reactive intermediates by angularly resolved PES and CIS, and TPE spectroscopy is important as, although extensive studies have been made of the photoionization behaviour of closed-shell atoms and molecules, few attempts have been made to investigate the photoionization dynamics of open-shell atoms and molecules because they are often difficult to prepare in sufficient number densities. However, these preparative problems have now been overcome by using techniques developed by the Southampton group and other research groups. Studying reactive intermediates, particularly open-shell reactive intermediates, in this way allows an investigation of effects such as electron correlation, and inter- and intra-channel coupling, and provides important tests of theories that take these interactions into account.

Table 2

The examples considered in the next section, the Case Studies, have been selected from the reactive intermediates studied by the Southampton group with synchrotron radiation (see Table 1, refs (23-43)). The aim of this section is to select examples which emphasize the main information to be obtained. The photoelectron spectrometers developed to study reactive intermediates and other experimental details are not described, although it is important to note that all the experiments considered have been made with a spectrometer which incorporates a hemispherical electrostatic electron energy analyser. Similarly the

theoretical methods used to interpret the spectra are not discussed in detail. However, essential experimental and theoretical information will be given, as required, in the Case Studies considered. In section 3, possible directions of future work are discussed by summarising recent photoelectron-photoion coincidence (PEPICO) and threshold photoelectron-photoion coincidence (TPEPICO) studies on reactive intermediates from other groups, see Table 2 refs (44-61). The information derived from the studies described in sections 2 and 3 is compared with a view to combining the advantages of both types of measurement in future studies. References to earlier studies by PES (62-78) using fixed energy photon sources derived from inert gas discharges are also included in Tables 1 and 2.

Figure 2

2. Case Studies

2.1 PES and CIS of some small molecules

2.1.1 O₂(¹Δ_g) (29,31)

Interaction of O₂ with vuv radiation has received considerable attention, partly because of the importance of photoexcitation and photoionization of O₂ in the earth's atmosphere. The ground electronic configuration of O₂ is

$$1\sigma_g^2 1\sigma_u^2 2\sigma_g^2 2\sigma_u^2 3\sigma_g^2 1\pi_u^4 1\pi_g^2$$

This gives rise to the states X³Σ_g⁻, a¹Δ_g and b¹Σ_g⁺. The first excited state, a¹Δ_g, is 0.98 eV above the ground state, X³Σ_g⁻, and both the X and the a states are important atmospheric constituents. O₂ a¹Δ_g is present in relatively high partial pressures in the troposphere, being produced with O(¹D) from photolysis of ozone, and is one of the strongest contributors to the airglow. Also, photoionization of O₂(¹Δ_g) has been suggested as an important source of ions in the D region of the atmosphere, to explain both the O₂⁺ partial pressures and the total ion densities at these altitudes.

O₂ a¹Δ_g can be prepared for laboratory studies by microwave discharge of a flowing mixture of molecular oxygen diluted in an inert gas. The absorption spectrum of O₂(a¹Δ_g) in the vuv region, recorded and analysed by Katayama, Huffman and co-workers (80-82), provides valuable background information. In this spectrum, a vibrationally resolved band at ~ 14.0 eV excitation energy was assigned to excitation to a 3s Rydberg state, a

$O_2(C^2\Phi_u, 3s\sigma_g) p^1\Phi_u v' \leftarrow O_2(^1\Delta_g)$, $v''=0$ resonance. Some vibrational components of this band were rotationally resolved and more intense than others; this effect was attributed to a vibrationally dependent competition between autoionization and predissociation in the excited state.

The PE spectrum of $O_2(X^3\Sigma_g^-)$ recorded with a helium discharge photon source (HeI, 21.22 eV) shows five bands, which correspond to ionization to the O_2^+ states $X^2\Pi_g$, $a^4\Pi_u$, $A^2\Pi_u$, $b^4\Sigma_g^-$ and $B^2\Sigma_g^-$. Removal of a $1\pi_g$ electron gives the $O_2^+ X^2\Pi_g$ state, removal of the $1\pi_u$ electron gives the $a^4\Pi_u$ and $A^2\Pi_u$ states, and the $b^4\Sigma_g^-$ and $B^2\Sigma_g^-$ states arise from removal of a $3\sigma_g$ electron. For $O_2(a^1\Delta_g)$, electron removal from the $1\pi_g$ level gives $O_2^+ X^2\Pi_g$, while loss of an electron from the $1\pi_u$ level gives the states $O_2^+ (C^2\Phi_u)$ and $(A^2\Pi_u)$, and the $(3\sigma_g)^{-1}$ ionization gives $O_2^+ (D^2\Delta_g)$. By recording a PE spectrum of discharged oxygen, as well as a spectrum with the discharge off, well-resolved $O_2(^1\Delta_g)$ photoelectron bands have been obtained for the ionizations $O_2^+ (X^2\Pi_g) \leftarrow O_2(^1\Delta_g)$, $O_2^+ (A^2\Pi_u) \leftarrow O_2(^1\Delta_g)$, $O_2^+ (C^2\Phi_u) \leftarrow O_2(^1\Delta_g)$ and $O_2^+ (D^2\Delta_g) \leftarrow O_2(^1\Delta_g)$.

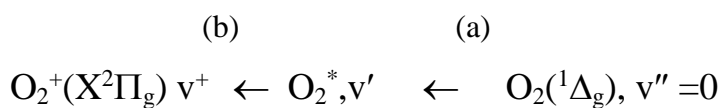
A HeI (21.22 eV) photoelectron spectrum recorded for an oxygen discharge is shown in Figure 2, with the assignment of the major features indicated in the caption. The 0.98 eV excitation energy of $O_2(a^1\Delta_g)$ relative to $O_2(X^3\Sigma_g^-)$ means that the first four vibrational components of the $O_2^+ (X^2\Pi_g) \leftarrow O_2(^1\Delta_g)$ band (labelled 1 in Figure 2) are observed before the onset of the more intense $O_2^+ (X^2\Pi_g) \leftarrow O_2(X^3\Sigma_g^-)$ band (labelled 2 in Fig.2). Also observed are features due to oxygen atoms, labelled as 3 and 5. The second and third bands of $O_2(a^1\Delta_g)$, arising from ionization to the $A^2\Pi_u$ and $^2\Phi_u$ ionic states, occur in the regions labeled 4 and 6 in Fig.2. These bands are not resolved in Fig.2, but can be clearly observed if the discharge is pulsed and a phase-sensitive method is used to detect photoelectron signals in-phase and out-of-phase with the discharge (see Supplementary Information; Fig.SI2).

As the first four vibrational components of the $O_2^+ (X^2\Pi_g), v^+ \leftarrow O_2(^1\Delta_g), v'' = 0$ band do not overlap with the $O_2^+ (X^2\Pi_g), v^+ \leftarrow O_2(X^3\Sigma_g^-), v'' = 0$ PE band, CIS spectra can be readily recorded for these four components. The CIS spectra obtained in the photon energy region 14.0-15.0 eV are shown in Figure 3. As can be seen, two bands, labelled A and B, dominate this spectrum at 14.11 and 14.37 eV. It was not immediately obvious why only two intense bands were observed; they are approximately 2100 cm^{-1} apart, roughly twice the separation of the vibrational separation in any known excited state of O_2^+ , so they cannot represent consecutive vibrational levels in a Rydberg state. As already stated, the first two

excited states of O_2^+ accessible from $O_2(^1\Delta_g)$ by one-electron ionization are $O_2^+(A^2\Pi_u)$ and $O_2^+(C^2\Phi_u)$. Analysis of the vibrationally resolved $O_2^+(C^2\Phi_u) \leftarrow O_2(^1\Delta_g)$ PE band gave ionic state vibrational constants close to those obtained from the absorption spectrum in the spectral region 13.5-14.5 eV (80-82). Also, analysis of the $O_2^+(A^2\Pi_u) \leftarrow O_2(^1\Delta_g)$ PE band gave ionic state vibrational constants which showed poorer agreement with those obtained from the vuv absorption spectrum. This led to the conclusion that the two strong lines, A and B, correspond to transitions to vibrational levels of a Rydberg state with a $O_2^+(C^2\Phi_u)$ core with the difference in the upper state vibrational quantum numbers being +2. The above information, taken with evidence from the absorption spectrum (80-82), led to the assignment of the two vibrational components A and B at 14.11 and 14.37 eV to excitation to the $v' = 3$ and $v' = 5$ levels in the $p^1\Phi_u$ excited state. Closer inspection of Figure 3 shows that a weak transition to $v' = 7$ can also be seen in some CIS spectra. An unusual feature of the vuv absorption band is that the vibrational components appear alternately sharp and diffuse, and this is attributed to a competition between predissociation and autoionization in the vibrational levels of the $^1\Phi_u$ Rydberg excited state. It appears that in $v' = 3$ and $v' = 5$ in this state autoionization is significant whereas in the other vibrational levels predissociation is dominant. Three dissociative states, two $^1\Delta_u$ states and one $^1\Phi_u$ state, which cross the $^1\Phi_u$ potential curve have been proposed to account for this (29). Using the position of the first vibrational component in the vuv absorption spectrum and the measured PE value of the AIE for $O_2^+(C^2\Phi_u) \leftarrow O_2(^1\Delta_g)$ of 17.51 eV, an effective principal quantum number (n) of 1.90 for the Rydberg state can be determined. This would correspond to a 3s electron in the excited state, with a quantum defect (δ) of 1.1.

Figure 3

As outlined earlier, if CIS spectra only arise from autoionization processes then it is expected that they can be simulated using a product of Franck-Condon factors for the two steps involved i.e. (a) and (b)



where O_2^* is a Rydberg state with an $O_2^+(C^2\Phi_u)$ core. To obtain these Franck-Condon factors, each state was represented by a Morse potential specified using established values of

r_e , ω_e and $\omega_e x_e$ for $O_2(^1\Delta_g)$ and $O_2^+(X^2\Pi_g)$ and the corresponding values for $O_2(C^2\Phi_u, 3s\sigma_g)$ $p^1\Phi_u$ taken from the vuv absorption study (80-82) (which are in good agreement with those derived for $O_2^+(C^2\Phi_u)$ from the photoelectron spectrum). Franck-Condon factors were computed for steps (a) and (b) for v' values in the range 0-10 and a selected value of v^+ . For each value of v^+ , a simulated CIS spectrum was derived by multiplying the Franck-Condon factors for each step together. The results are shown as black circles in Fig.3. As can be seen, the fit between experimental and computed relative intensities is poor, with virtually no signal being observed in the experimental spectrum for any v' level other than $v' = 3, 5$ and 7 . This poor agreement is a consequence of competition between autoionization and predissociation in the $^1\Phi$ excited state. However, for the two clearly observed bands A ($v' = 3$) and B ($v' = 5$), the overall computed relative intensity trend, of A rising with respect to B as v^+ increases, is correct. If the $v' = 3$ level is predissociated slightly more efficiently than $v' = 5$, then the intensity of band A will be lower than calculated relative to band B, as is observed. Indeed in the vuv absorption spectrum (80-82), the $v' = 3$ absorption band is slightly less well resolved than the $v' = 5$ band and from the rotational linewidths in the absorption spectrum approximate lifetimes of the $v' = 3$ and $v' = 5$ levels may be estimated, after allowance for the instrumental contribution, as 1.8 and 2.6 ps respectively. If it is assumed that predissociation of the $v' = 5$ level is minimal, then 2.6 ps represents the autoionization lifetime of this level. Predissociation of the $v' = 3$ and $v' = 5$ levels is presumably relatively slow while for other vibrational levels it is much faster as little or no signals are seen for these levels in the CIS spectrum.

A PE spectrum of discharged oxygen recorded at a photon energy corresponding to bands B in Figure 3 (14.37 eV) is shown in Figure 4. Comparison with spectra recorded with the discharge off allowed contributions from $O_2(^1\Delta_g)$ and $O(^3P)$ to the discharge spectrum to be identified. Since in Figure 4 some of the photoelectron signals arising from ionization of $O_2(^1\Delta_g)$ are partly obscured by stronger signals arising from $O_2(X^3\Sigma_g^-)$, the $O_2(X^3\Sigma_g^-)$ features were subtracted from a spectrum recorded with the discharge on. The lowest trace in this figure shows the contribution from $O_2(^1\Delta_g)$, which represents the PE spectrum of $O_2(^1\Delta_g)$ at the photon energy used over the ionization energy region 10.0-14.5 eV, except between 13.5 and 13.7 eV ionization energy where contributions from molecular and atomic oxygen overlap, making accurate subtraction impossible. (The $O^+(^4S) \leftarrow O(^3P)$ ionization occurs at 13.61 eV). For the $O_2^+(X^2\Pi_g) \leftarrow O_2(^1\Delta_g)$ ionization, 16 vibrational components are observed

instead of the 4 vibrational components seen in the HeI (21.22 eV) photoelectron spectrum. (The spectrum recorded at a photon energy of 14.11 eV, the position of band A in Figure 3, is shown in the SI section, Figure SI3).

The $O_2(^1\Delta_g)$ PE spectrum in Figure 4 arises from two contributions (i) direct photoionization and (ii) autoionization from the resonant Rydberg state. Each of these processes will have an associated Franck-Condon envelope for population of the $O_2^+(X^2\Pi_g)$ state. For (i), Franck-Condon factors were calculated for the process $O_2^+(X^2\Pi_g) v^+ \leftarrow O_2(^1\Delta_g), v''=0$. For (ii), Franck-Condon factors were calculated for the process $O_2^+(X^2\Pi_g) v^+ \leftarrow O_2^*, v'$ (step (b) above). For each of the resonant photon energies of bands A and B in Figure 3, by using the intensity of the background in the CIS spectrum as the intensity of the direct photoionization contribution and the band intensity on resonance above the background in Figure 3 as the autoionization contribution, the respective Franck-Condon envelopes could be scaled and summed to yield the calculated photoelectron spectrum.

The vibrational component intensities obtained from this procedure are displayed as solid circles in Figure 4 (and Fig.SI3), where the resonant states were assumed to be $^1\Phi_u, v' = 3$ and $^1\Phi_u, v' = 5$ respectively. As can be seen the agreement between the experimental and simulated envelopes is good. For the $h\nu = 14.11$ eV PE spectrum, if the resonant Rydberg state is assumed to be $^1\Phi_u, v' = 2$ or 4 rather than $^1\Phi_u, v' = 3$, then poor agreement is obtained between the experimental and computed envelopes. Similarly, for the $h\nu = 14.37$ eV PE spectrum, good agreement between the experimental and simulated spectrum is only obtained for $v' = 5$ supporting the vibrational numbering of resonance levels given in the vuv absorption study and shown in Figure 3.

Figure 4

Angular distribution parameter (β) plots vs photon energy for the $O_2^+(X^2\Pi_g), v^+=0-3 \leftarrow O_2(^1\Delta_g), v''=0$ ionizations have been recorded in the photon energy range 13.8-15.2 eV (28). β shows maxima at energies corresponding to the autoionization resonances $O_2^*(p^1\Phi_u), v' \leftarrow O_2(^1\Delta_g), v''=0$, seen in Figure 3 with β being negative throughout this photon energy range but less negative at the resonant energies (see Fig.SI4). According to electric dipole selection rules, in the $O_2^+(X^2\Pi_g) + e^- \leftarrow O_2(^1\Delta_g) + h\nu$ ionization process, the

photoelectron can have σ_u , π_u , δ_u , and ϕ_u character. In a united atom picture, the highest occupied molecular orbital in $O_2(^1\Delta_g)$, a π_g orbital, becomes a d orbital, so the prominent components in the photoelectron wave are expected to be $l = 1$ (p) or $l = 3$ (f). (A pure $d \rightarrow f$ ionization is expected to have $\beta = 0.8$ and a pure $d \rightarrow p$ ionization is expected to have $\beta = 0.4$). This result can be compared with the selection rules which apply to autoionization from the $^1\Phi_u$ excited state. Autoionization cannot change the overall state symmetry, so the ion plus free electron must also have $^1\Phi_u$ symmetry. Since the ionic state is $^2\Pi_g$, the photoelectron must have δ_u or γ_u symmetry which cannot be obtained from a $l = 1$ (p) free electron wave but δ_u can be obtained from a $l = 3$ (f) wave. Therefore, it is expected that the relative f contribution to the photoelectron wave will increase at the resonant photon energies, as the p contribution can only arise from direct ionization and not autoionization. It is expected, therefore, that on changing the photon energy from an off-resonant to an on-resonant position, the free electron photoionization cross-section ratio $\sigma_f : \sigma_p$ will increase. The phase shift, Δ , between the photoelectron waves will also change between resonant and non-resonant photon energies. Unfortunately, however, neither Δ nor the ratio $\sigma_f : \sigma_p$ at resonant and non-resonant photon energies, can be quantified from the present measurements. Using the angular momentum transfer treatment of Dill (83), with the experimental evidence that the β values change from negative values off-resonance to less negative values on-resonance, indicates that parity unfavoured transitions, for which $\beta = -1$, are less prominent at the resonance positions. However, this angular momentum transfer method, which we have used to analyse the angular distribution PE measurements of iodine atoms (see section 2.3 later), cannot be applied in full to the $O_2(^1\Delta_g)$ case because the number of open channels is too large. (a definition of parity favoured and unfavoured transitions is given in section 2.3). However, the angular distribution plots (Figure SI4) do reproduce the structure shown in Figure 3, and indicate that the f contribution to the photoelectron wave increases at the resonant energies, notably at 14.11 and 14.37 eV.

In summary, two strong resonances have been observed in the CIS spectra recorded for $O_2(^1\Delta_g)$. At these photon energies there is an enhancement in the photoionization cross section of $O_2(^1\Delta_g)$ and PE spectra recorded at these energies allow extra vibrational structure to be obtained. At $h\nu = 14.37$ eV, the $O_2(^1\Delta_g)$ PE features are comparable in intensity to the $O_2(X^3\Sigma^-_g)$ PE features (see Figure 4) even though the partial pressure ratio is $\sim 1:7$ ($^1\Delta_g :$

$X^3\Sigma^-_g$). This implies that the $O_2(^1\Delta_g)$ photoionization cross section is nearly an order of magnitude greater than the $O_2(X^3\Sigma^-_g)$ photoionization cross section at this photon energy. This example demonstrates the advantage of recording PE spectra at a photon energy on a resonance to give enhanced intensity and extra vibrational structure.

2.1.2 SO ($X^3\Sigma^-$) (26,27)

Related studies have also been made on SO, a reactive intermediate which is important in atmospheric chemistry and astrophysics. It is produced in the earth's stratosphere via photodissociation of SO_2 , the main anthropogenically produced sulphur containing air pollutant, and it is a known intermediate in chemical reactions in the earth's troposphere. Also, molecules with sulphur content account for ~10% of the species in the interstellar medium and planetary atmospheres, and of these SO is the most abundant. SO^+ is also important in astrochemistry. It has been detected in interstellar molecular clouds, and in the plasma torus of Jupiter in the orbit of Io, one of Jupiter's satellites.

Figure 5

SO is valence isoelectronic with O_2 and its ground state ($X^3\Sigma^-$) electronic configuration is $---6\sigma^27\sigma^22\pi^43\pi^4$. The 3π , 2π and 7σ orbitals are accessible with 21.22 eV radiation. The $(3\pi)^{-1}$ ionization gives the $SO^+ X^2\Pi$ state, the $(2\pi)^{-1}$ ionization gives the $SO^+ a^4\Pi$ and $A^2\Pi$ states, and the $(7\sigma)^{-1}$ ionization gives $SO^+ b^4\Sigma^-$ and $B^2\Sigma^-$ states. Ionizations to all five ionic states have been observed as vibrationally resolved bands in the HeI photoelectron spectrum (62). SO can be prepared for spectroscopic study by microwave discharge of flowing SO_2 diluted in argon. Figure 5 shows photoelectron spectra obtained with the discharge on and off. The first and fourth SO bands at 10.30 and 14.94 eV vertical ionization energies (VIEs), corresponding to the ionizations $SO^+ (X^2\Pi) \leftarrow SO(X^3\Sigma^-)$ and $SO^+ (b^4\Sigma^-) \leftarrow SO(X^3\Sigma^-)$ respectively, can be clearly seen on comparing these spectra. CIS spectra have been recorded for vibrational components of the first band and results similar to those described for $O_2(^1\Delta_g)$ have been obtained. CIS spectra were also recorded for the fourth band, in the photon energy region 15.0-16.4 eV. This energy region is above the fourth but below the fifth AIE of SO. CIS spectra obtained for the $SO^+ b^4\Sigma^-$, $v^+=0$ and $SO^+ b^4\Sigma^-$, $v^+=1$ levels in this photon energy range are shown in Figure 6. In each case, both positive and negative resonance features were observed on top of a gradually rising

background. These sharp features arise from excitation to Rydberg states which converge to $\text{SO}^+ \text{B}^2\Sigma^-$ and autoionize to $\text{SO}^+ \text{b}^4\Sigma^-$. Fitting the position of the positive resonances in Figure 6 for the $v^+ = 0$ spectrum to the Rydberg energy expression,

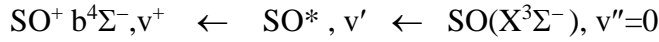
$$\text{Ex.En} = \text{IE} - \frac{R}{(n - \delta)^2}, \text{ gave } \delta = 0.12 \text{ and IE} = 16.43 \text{ eV, consistent with excitation to states}$$

with a Rydberg orbital which is oxygen d in character. (In this equation Ex.En is the excitation energy (or position) of the positive resonances, IE is the SO fifth AIE, R is the Rydberg constant, n is the principal quantum number and δ is its quantum defect; see also equation 10, which appears later). Similarly fitting the position of the negative resonances in the $v^+ = 0$ spectrum gave $\delta = 0.52$ and $\text{IE} = 16.43 \text{ eV}$, consistent with excitation to states with a Rydberg orbital which is oxygen p in character (26,27). The fifth AIE determined from these fits, 16.43 eV , is in good agreement with the value determined from the earlier PES work of $(16.44 \pm 0.02) \text{ eV}$, obtained from measurements involving deconvoluting overlapping SO and SO_2 features (62). The $\text{SO}^+ \text{b}^4\Sigma^-, v^+ = 1$ CIS spectrum is similar to the $\text{SO}^+ \text{b}^4\Sigma^-, v^+ = 0$ CIS spectrum but with each resonance feature shifted to higher energy by $(970 \pm 40) \text{ cm}^{-1}$ (see Fig.6). This separation is close to the value of $(1000 \pm 40) \text{ cm}^{-1}$ obtained for the vibrational constant ω_e in $\text{SO}^+ \text{B}^2\Sigma^-$ in the original PES study (62), consistent with excitation to $v' = 0$ (in Fig 6(a)) and $v' = 1$ (in Fig.6(b)) vibrational components of Rydberg states which are parts of series converging to $\text{SO}^+ \text{B}^2\Sigma^-$.

Figure 6

The positive and negative resonances observed in Figure 6, known as Fano profiles, arise from interaction of the excited Rydberg state with the continuum, with the shape of each observed resonance depending on the nature and extent of the interaction. The fact that the oxygen d resonances are positive and the oxygen p resonances are negative reflects the different nature of the interactions of the corresponding SO^* Rydberg states with the $\text{SO}^+ \text{b}^4\Sigma^-$ continuum, in particular the Fano q and p parameters will be substantially different for these two states. Unlike the structure shown in the CIS spectrum of $\text{O}_2(^1\Delta_g)$ (Fig. 3), only one vibrational component was observed for each principal quantum number, n , in a given series. This arises because $\text{SO}^+ \text{b}^4\Sigma^-$, and $\text{SO}^+ \text{B}^2\Sigma^-$, as well as Rydberg series which converge to

$\text{SO}^+ \text{B}^2\Sigma^-$, have very similar spectroscopic constants (r_e , ω_e and $\omega_e x_e$) and potential energy curves which are essentially the same, at least in the region of low vibrational levels ($v^+, v' \leq 4$), but displaced by a constant energy separation. Franck-Condon factors for autoionization between a resonant Rydberg state, which is part of a series that converges to $\text{SO}^+ \text{B}^2\Sigma^-$, and $\text{SO}^+ \text{b}^4\Sigma^-$ are therefore, expected to be essentially diagonal (i.e. ionizations with $\Delta v = 0$ have Franck-Condon factors close to unity and ionizations with $\Delta v \neq 0$ are close to zero). Hence CIS spectra recorded for the $\text{SO}^+ \text{b}^4\Sigma^-, v^+ = 0$ vibrational state will only show appreciable intensity from the $v'=0$ vibrational levels in the resonant Rydberg states. A $\Delta v=0$ propensity rule will also hold for the $\text{SO}^+ \text{b}^4\Sigma^-, v^+ = 1$ CIS spectra. This expectation has been confirmed by Franck-Condon factors calculated for selected v^+ levels for the process



where SO^* is a Rydberg state with a $\text{SO}^+ \text{B}^2\Sigma^-$ core (i.e. $\text{SO}^* \text{B}^2\Sigma^-, n\lambda$).

The CIS spectra in Figure 6 allow resonance energies to be chosen which will selectively enhance vibrational components of the fourth photoelectron band of SO. For example, because the Franck-Condon factors between $\text{SO}^+ \text{B}^2\Sigma^-$ and $\text{SO}^+ \text{b}^4\Sigma^-$ are diagonal, photoelectron spectra recorded for the fourth SO band at a photon energy corresponding to a $\text{SO}^* \text{B}^2\Sigma^-, nd, v' = 0$ resonance are expected to give enhancement of the first vibrational component in the fourth photoelectron band. Also, photoelectron spectra recorded for the fourth SO band using a photon energy on a $\text{SO}^* \text{B}^2\Sigma^-, nd, v' = 1$ resonance are expected to give enhancement of the second vibrational component. Figure 7(a) shows a photoelectron spectrum of the fourth band of SO recorded at a photon energy of 21.218 eV, a photon energy at which only direct ionization occurs. Figure 7(b) shows a photoelectron spectrum of the fourth band recorded at a photon energy of 15.535 eV. This corresponds to a positive resonance in Fig.6, the $\text{SO}^* \text{B}^2\Sigma^-, 4d, v' = 0$ resonance, and is not a resonance in the $v^+=1$ CIS spectrum. As a result, the photoelectron spectrum in Figure 7(b) shows, as expected, a large signal from the $v^+ = 0$ component with very little signal from the $v^+ = 1$ and 2 components. Other examples of photoelectron spectra recorded at different resonant photon energies are shown in this figure. Figure 7(c) shows a photoelectron spectrum of the fourth band recorded at a photon energy of 15.855 eV. This corresponds, within the photon bandwidth of 5 meV, to a positive resonance in the $\text{SO}^+ \text{b}^4\Sigma^-, v^+=0$ spectrum and a negative resonance in the $\text{SO}^+ \text{b}^4\Sigma^-, v^+=1$ CIS spectrum. As expected, an enhancement of the first vibrational component and a decrease in the second component of the fourth photoelectron band was obtained. In contrast, a spectrum obtained at a photon energy of 15.970 eV (Figure

7 (d)), which corresponds, within the photon bandwidth, to a positive resonance in the $\text{SO}^+ \text{b}^4\Sigma^-, v^+ = 1$ CIS spectrum and a negative resonance in the $\text{SO}^+ \text{b}^4\Sigma^-, v^+ = 0$ CIS spectrum, shows the expected enhancement of the second vibrational component.

Figure 7

These studies on $\text{O}_2(^1\Delta_g)$ and $\text{SO}(\text{X}^3\Sigma^-)$ suggest a general strategy of obtaining extra information on the photoionization behaviour of a reactive intermediate, with synchrotron radiation. It involves (i) recording a PE spectrum at a vuv photon energy which gives only direct ionization, (ii) recording CIS spectra for each observed vibrational component in the PE spectrum and noting the vuv photon energies where resonances are observed, and then (iii) recording PE spectra at selected resonant photon energies. These examples also indicate that likely applications of these PES and CIS methods to reactive intermediates will include the determination of vibrational constants of their molecular ionic states and preparation of their molecular ions in vibrationally selected states for ion-molecule kinetic studies. As well as $\text{O}_2(^1\Delta_g)$ and $\text{SO}(\text{X}^3\Sigma^-)$, these methods have been used to study a number of other reactive molecules notably CS, OH, OD, SH, NO and CF (refs.28,30,34,36,37). This has allowed measurement of first and higher ionization energies, derivation of ionic state vibrational constants, analysis of Rydberg series and determination of the atomic characters of the excited Rydberg orbitals, and investigation of photoionization dynamics through angular distribution measurements.

2.2 TPES of some small molecules

In threshold photoionization, an atom or molecule is ionized using a photon with energy just above the atomic or molecular ionization threshold. Photoelectrons are produced with energies that are typically in the range from zero to a few meV, and in TPES the intensities of these threshold electrons are measured using electron analysers, tuned to these low energies, with a suitable detector. Whilst PES is the study of the intensity and energy distribution of electrons produced from an atomic or molecular target at fixed photon energy, which is usually well above an ionization threshold, TPES is the study of the intensity of low energy photoelectrons (typically < 2 meV) as the photon energy is scanned. A threshold photoelectron signal will be obtained each time the photon energy is equal to the ionization energy to an ionic state. Whilst the observed intensities of vibrational components in a PE

spectrum of a molecule are almost always governed by Franck-Condon factors (FCFs) between the initial neutral and final ionic states, those observed by TPES often have significant contributions from autoionization (84,85), and this may lead to extra vibrational components of an ionic state to be observed in TPES.

2.2.1 CF₂ (39)

Difluorocarbene, CF₂, is important in plasma processing and is produced in the stratosphere by photodissociation of chlorofluorocarbons by radiation from the sun. CF₂ and other small reactive intermediates play important roles in determining the etch rate, selectivity and anisotropy of plasma-etching processes. It has been found that the primary mechanism for production of CF_x reactive intermediates (where $x = 1,2,3$) is neutralisation and fragmentation of CF_x⁺ ($x = 1-4$) ions incident on the powered electrode of a plasma etcher rather than direct electron-impact induced fragmentation of the feedstock gas (86). The first AIE of CF₂ is important in determining the enthalpy of ion-molecule reactions involving CF₂⁺ in plasmas. Previous determinations of the first AIE of CF₂ have been by PES (13), which gave the first AIE as (11.42 ± 0.01) eV, by PIMS (87), using a synchrotron source, which gave the first AIE as (11.445 ± 0.025) eV, and a study by electron impact mass spectrometry, which gave a value of (11.5 ± 0.4) eV (88). In the PES study (13), the first band of CF₂ consisted of extensive vibrational structure, with at least 15 components being observed. It was interpreted (13) as a regular series in the deformation mode in the ionic state. The vertical ionization energy (VIE) was measured as (12.240 ± 0.005) eV. This band has been re-investigated at higher resolution using TPES. The objective was to obtain a higher resolution spectrum of the first band in order that the first AIE could be determined more reliably than previously and the vibrational structure in the first band could be analysed more thoroughly.

In the recent PES and TPES study (39), CF₂ was produced by microwave discharge of flowing hexafluoropropene, C₃F₆, diluted in argon. This gives rise to almost complete destruction of C₃F₆ with production of CF₂ and C₂F₄. The CF₂ first PE band, which occurs in the ionization energy region 11.3-13.2 eV, is highly structured. Figure 8 shows the TPE spectrum of CF₂ recorded in this photon energy region (upper part of Fig.8), together with a PE spectrum recorded at a photon energy of 21.0 eV (lower part of Fig.8). As expected, the TPE spectrum has better resolution than the PE spectrum. It also has a very different vibrational profile to the Franck-Condon distribution of the PE spectrum because of

autoionization effects in the TPE spectrum. In the TPE spectrum the lower vibrational bands are more intense and more clearly resolved than in the PE spectrum. In the first PE study of CF₂ (13), the AIE and VIE were determined as 11.42 ± 0.01 eV and 12.240 ± 0.005 eV respectively. In the more recent TPE study (39), it is possible to measure the VIE from the PE spectrum as 12.258 ± 0.002 eV and the lowest vibrational component observed in the TPE spectrum is measured as 11.438 ± 0.004 eV. In both cases the shift with respect to the previous PE study (13) is 18 meV to higher ionization energy. From the experimental TPE spectrum, it is not possible to establish if the vibrational component observed at 11.438 eV is really the lowest vibrational component. This is because below 11.4 eV there is a contribution from the highest observed vibrational component of the first PE band of C₂F₄ (see Fig. SI5). Also, although in the TPE spectrum in Figure 8 it is possible to observe some structure below 11.4 eV, the signal-to-noise is not sufficient to allow unambiguous identification of possible weak vibrational components of CF₂ and weak C₂F₄ contributions. For this reason the first PE band of CF₂ was computed using an *ab initio*/Franck-Condon method. This involves computing potential energy functions (PEFs) for CF₂ and CF₂⁺ using high level electronic structure calculations, and then using the PEFs to obtain vibrational wavefunctions for each state, via solution of a Schrödinger equation with an appropriate Hamiltonian. Franck-Condon factors between the ground neutral and ionic state were then computed using these vibrational wavefunctions. The method, which is described in the original paper (39), includes Duschinsky rotation and anharmonicity. It was anticipated that the overall envelope in the TPE spectrum, which was of higher resolution than the PE spectrum, would not be reproduced in these Franck-Condon calculations and this proved to be the case. However, the TPE vibrational components that showed partially resolved structure, from vibronic transitions which are close in energy, were reproduced by these calculations. This allowed correct positioning of the simulated spectrum on the ionization energy scale and hence determination of the AIE.

Figure 8

The experimental TPE spectrum was compared with the simulated CF₂⁺ (X²A₁) ← CF₂(X¹A₁) photoelectron spectrum with an initial neutral Boltzmann distribution at a vibrational temperature of 0 K (see Figure 9). This was done by positioning the computed envelope so that the structure within the higher components in the TPE spectrum matched well with the computed structure, notably in the third, fourth, sixth and ninth

components (see Figures 9 and SI6). The spectral simulation used a Gaussian function of width 5 meV for each vibrational component that is comparable with the experimental resolution. The adiabatic component obtained from positioning the computed envelope in this way is 11.367 eV. This component has a very small relative intensity and it is below the noise level of the experimental TPE spectrum. The positions of all the observed vibrational components are in excellent agreement with the computed components although the TPE overall vibrational envelope is different from the computed envelope. This is because of the non-Franck-Condon behaviour of threshold photoionization. However, the shape of each experimental vibrational component closely matches the shape of the corresponding calculated vibrational component as can be seen from the comparison of the lowest vibrational components shown in Figure 9. In the third, sixth and eleventh experimental vibrational components (counting the 11.36 eV component as the first), it is possible to observe two features with the one at lower ionization energy more intense; the same pattern is observed in the calculated vibrational components. The fourth, seventh and ninth experimental vibrational components each show two features with the one at higher ionization energy more intense; the same pattern is observed in the calculated fourth and seventh vibrational components while in the ninth component the two contributing features are comparable in intensity. In the other calculated vibrational components in Figure 9, the 5 meV band-width used is not good enough to allow separation of different components and the same is true for the corresponding experimental vibrational components which appear to be a single feature. The exception is the weak vibrational component at 11.45 eV in Figure 9 which is a single vibrational component in the calculated spectrum while it appears to have two components in the experimental spectrum.

Figure 9

The simulation of the band envelope has been repeated using an initial neutral Boltzmann distribution at a vibrational temperature of 600 K and the result is shown in Figure 10 (and Fig.SI7). (It is expected that CF₂ will be vibrationally excited under the conditions used and the Boltzmann vibrational temperature of 600 K was selected as it gave the best fit for the structure in the low energy vibrational components, notably for the band at 11.45 eV). The main differences with respect to the simulation at 0 K are at ionization energies above 12.8 eV and for the vibrational component in Figure 9 at \approx 11.45 eV. This band, in the simulation

at 600 K, has a “hot band” on the higher ionization energy side as can be seen in Figure 10. The shape of the 11.45 eV vibrational component in the experimental TPE spectrum in Figure 9 is therefore explained by including a contribution from a “hot” band. The simulated spectrum at 600 K (Figure 10) offers a better match with the experimental spectrum than the simulated spectrum at 0 K (Figure 9), with respect to the vibronic structure associated with each component, notably for the fourth, sixth and ninth vibrational components (counting the component at 11.36 eV as the first).

Figure 10

The ionization energies of the calculated vibrational components from the *ab initio*/Franck-Condon factor calculations are on average 5 meV higher than the more intense experimental vibrational components in the 11.6-12.6 eV region. Hence, by moving the computed bands down by 5 meV to match the more intense experimental TPE vibrational component positions, the AIE is determined to be 5 meV lower than the value obtained from the simulation. This gives a value of 11.362 ± 0.005 eV for the AIE.

An overview of the assignment of the main structure in the experimental TPE spectrum in the photon energy region 11.3-12.2 eV is shown in Figure 11. As can be seen, the main structure shown corresponds to $(v_1^+, v_2^+, 0) \leftarrow (0, 0, 0)$ combination bands with v_1^+ and $v_2^+ = 0, 1, 2$ and 3. The doublet structure observed in some of these bands arises because $2v_2^+$ is approximately equal to v_1^+ . On comparing Figure 11 with the experimental TPE spectrum in the photon energy region 11.4-12.2 eV (Figure 10), and using the information provided by the simulations, the doublet structure observed in the experimental vibrational components can be assigned. For example, in the first two observed components at 11.45 and 11.52 eV the doublet structure can be assigned to the $(0, 1, 0) \leftarrow (0, 0, 0)$ and $(1, 0, 0) \leftarrow (0, 1, 0)$ ionizations, and the $(0, 2, 0) \leftarrow (0, 0, 0)$ and $(1, 2, 0) \leftarrow (1, 0, 0)$ ionizations respectively. Also, the doublet structure in the band at 11.77 eV can be assigned to the ionizations $(1, 3, 0) \leftarrow (0, 0, 0)$ and $(2, 1, 0) \leftarrow (0, 0, 0)$.

Once the main assignments of the structure in the experimental TPE spectrum have been established, values of the vibrational constants v_1^+ (symm. stretching mode) and v_2^+ (symm. bending mode) in the ionic state can be derived. For v_1^+ , ω_e and $\omega_e x_e$ were obtained as (1370 ± 20) and $(7 \pm 10) \text{ cm}^{-1}$. For v_2^+ , the corresponding ω_e and $\omega_e x_e$ values obtained from the experimental TPE spectrum are $(635 \pm 10) \text{ cm}^{-1}$ and $(0 \pm 5) \text{ cm}^{-1}$.

Figure 11

In summary, in the TPE spectrum of CF₂ extensive vibrational structure was obtained for this band but the adiabatic component was not observed. Even though the TPE vibrational envelope is non-Franck-Condon in nature, comparison of the structure associated with the vibrational components with that expected from an *ab initio*/Franck-Condon simulation has allowed the ionic state vibrational quantum numbers associated with each observed vibrational component to be determined. The position of the adiabatic component was determined as 11.362 ± 0.005 eV. Also, the harmonic and fundamental vibrational frequencies for ν_1^+ and ν_2^+ for CF₂⁺(\tilde{X}^2A_1) have been derived from the experimental TPE spectrum. These compare well with those determined from the potential energy function for CF₂⁺(\tilde{X}^2A_1) computed with high level electronic structure calculations.

2.2.2 IF (23)

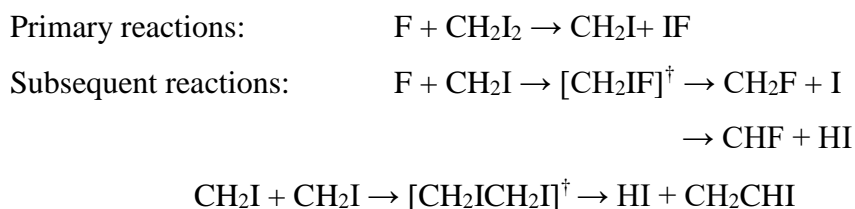
IF is a short-lived molecule in the gas-phase which typically has a lifetime of several milliseconds in a low pressure flowing gas system. It has been shown to be a promising candidate for a visible chemical laser via energy transfer to its vibrationally excited ground state, IF(X¹Σ⁺), from O₂(a¹Δ_g) to produce IF(B³Π) (89-91).

In an initial study by PES (71), IF was produced from the rapid gas-phase reaction F + ICl → IF + Cl. However, because of the minor reaction channel F + ICl → FCl + I, I atoms were also observed in the spectra and some of the I atom features overlapped with some of the vibrational components in the first two IF PE bands. For these overlapped bands, the relative contributions of I and IF were not established.

In the second study of IF (23) the main objective, therefore, was to determine these contributions so that reliable vibrational envelopes of the PE bands of IF and the relative intensities of I atom bands could be obtained. It was also proposed to obtain the TPE spectrum of IF once these goals had been achieved. The PE and TPE spectra of the stable halogens and interhalogens F₂, Cl₂, Br₂, ICl and IBr have been recorded previously (92-95). In these cases, the TPE spectra are notable in that extra vibrational structure is observed in the first TPE bands, compared to the structure seen in the PE spectra. In the second study of IF, the F + CH₂I₂ reaction was used as the source of I and IF (23), and spectra were obtained at different reaction times to obtain PE spectra for different partial pressures of I and IF. These spectra were then

used to obtain “pure” PE spectra of both I and IF. Once these PE spectra had been obtained, TPE spectra were then recorded.

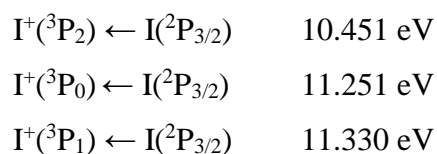
The F + CH₂I₂ reaction produces a number of reactive intermediates. The primary and secondary reactions involved are shown below:-



In an earlier PES study of this reaction by the Southampton group (79), CH₂I, produced by the primary reaction, was observed at low mixing distances (≈ 0.3 cm) above the photon beam (at 8.52 eV VIE) whereas only bands from I, IF, HI, HF, CH₂CHI (vinyl iodide) and CF (weakly) were observed at longer mixing distances (≈ 3 -4 cm) (longer reaction times). The reactive intermediates CH₂F and CHF in the above reaction sequence are converted, by further fluorine atom H-abstraction, to CF + HF at the relatively long reaction times. Known PE spectra of CF, HI, HF, and CH₂CHI were checked and it was found that they do not contribute significantly to the spectral region investigated. CH₂I₂ also does not contribute to the spectra as it was almost completely removed in the primary reaction step.

IF has the electronic configuration $---12\sigma^2 6\pi^4 13\sigma^2 7\pi^4$. In the initial study with PES (71), the first two bands were vibrationally resolved. They correspond to ionization to the $^2\Pi_{3/2}$ and $^2\Pi_{1/2}$ ionic states at VIEs of 10.62 and 11.32 eV respectively arising from the $(7\pi)^{-1}$ ionization. The $(13\sigma)^{-1}$ and $(6\pi)^{-1}$ ionizations gave rise to broad bands at VIEs of 15.22 and 15.94 eV respectively which showed no vibrational structure (71).

The ground state electronic configuration of atomic iodine is $---5s^2 5p^5$. This gives rise to two states $^2P_{3/2}$ and $^2P_{1/2}$ separated by 0.94 eV with the $^2P_{3/2}$ state lower (96). The $^2P_{1/2}$ state is effectively not populated under equilibrium conditions at room temperature. The $(5p)^{-1}$ ionization from the $^2P_{3/2}$ ground state is expected to give 3P_2 , 3P_1 , 3P_0 , 1D_2 and 1S_0 ionic states with the following ionization energies determined from photoabsorption measurements (97,98):-



$$\text{I}^+(^1\text{D}_2) \leftarrow \text{I}(^2\text{P}_{3/2}) \quad 12.153 \text{ eV}$$

$$\text{I}^+(^1\text{S}_0) \leftarrow \text{I}(^2\text{P}_{3/2}) \quad 14.109 \text{ eV}$$

Figure 12 shows part of a PE spectrum recorded for the $\text{F} + \text{CH}_2\text{I}_2$ reaction, in the ionization energy region from 10.3 eV to 12.3 eV using a reactant mixing distances of 3 cm above the photon beam. The selected photon energy from the synchrotron was 21.22 eV and the spectra were recorded at an angle of $54^\circ 44'$ with respect to the direction of polarization of the photon beam. (This angle corresponds to the angle at which the intensity measurement is independent of the angular distribution parameter, β , thereby, permitting a straightforward determination of the relative partial cross section.)

In Figure 12 the intensities of the atomic I spectral features are relatively low, compared to the intensity of the IF features, but this ratio increased at higher mixing distances (longer reaction times).

Figure 12

As can be seen in Figure 12, two groups of bands were observed in the regions 10.35-10.80 eV and 11.25-11.55 eV with a single band at 12.15 eV. To assist the analysis, these were labelled (a'-e'), (a-d) and a'' as shown. The assignment of these bands follows that reported in the initial PE study of IF (71). Bands (b') to (e') are vibrational components of the first IF band ($\text{IF}^+ (^2\Pi_{3/2}) \leftarrow \text{IF} (^1\Sigma^+)$) from the $(7\pi)^{-1}$ ionization), and bands (a) to (d) are vibrational components of the second IF band ($\text{IF}^+ (^2\Pi_{1/2}) \leftarrow \text{IF} (^1\Sigma^+)$) from the $(7\pi)^{-1}$ ionization). However, for bands (a) and (b), the relative contributions from I and IF were not known. It was also not known whether or not IF contributes to band (a').

By investigating spectra with different I:IF ratios, it was found that bands a' and a'' are I atom ionizations, bands b'-e' are vibrational components of the first band of IF, bands c and d are vibrational components of the second band of IF and bands a and b contain both I atom and IF second band contributions (23). By analysing many spectra with different I:IF ratios (23), it was possible to obtain the I relative band intensities and the IF vibrational component relative band intensities (see Table SI1 and Figs SI8 and SI9). The AIEs, VIEs and ionic vibrational constants obtained for the two IF bands are shown in Table 3.

Spectra with different I:IF ratios were obtained by recording PE spectra at different mixing distances. It was also possible to obtain different I:IF ratios at the same mixing distance by recording PE spectra at different times; for example, when the reaction had just been started

and after the reaction had been running for some time. This was possible since the I atom intensity decreased with respect to IF over the timescale of several hours, probably because of the change in efficiency in wall recombination of I atoms with time.

The TPE spectrum recorded for the $F + CH_2I_2$ reaction in the 10.3 - 12.3 eV photon energy region at 3 cm mixing distance above the photon beam is shown in Figure 13. Comparing this TPE spectrum with the PE spectrum shown in Figure 12, it can be seen that better resolution is obtained for the TPE spectra and, as expected, different relative band intensities are observed. All the atomic I features (i.e. bands a', a'', and contributions to bands b, a) have increased in relative intensity with respect to the IF bands compared to the relative intensities seen in the PE spectra. This is particularly the case for band (a'), the first iodine atom ionization, $I^+(^3P_2) \leftarrow I(^2P_{3/2})$, and this has been attributed to an autoionization resonance 2.5 meV above threshold (23).

Comparison of Figures 12 and 13 also shows that the relative intensities of vibrational components in each $IF^+ \leftarrow IF$ band are similar in both the TPE and PE spectra. In particular higher vibrational members of the first IF photoelectron band are not observed in the TPE spectrum in the “non-Franck-Condon region” between the $IF^+(X^2\Pi_{3/2}) \leftarrow IF(X^1\Sigma^+)$ and $IF^+(^2\Pi_{1/2}) \leftarrow IF(X^1\Sigma^+)$ bands, indicating an absence of significant autoionization to these higher vibrational states. This is in contrast to TPE spectra of the stable halogens and interhalogens F_2 , Cl_2 , Br_2 , ICl and IBr (92-95) where extra vibrational structure is observed, which is not seen in the PE spectrum, in the “Franck-Condon gap” between the first and the second bands.

Figure 13

The TPE and PE spectra of the first two bands of IF were used to obtain the positions of each vibrational component (see Table SI2) and the PE spectrum was used to obtain the vibrational component relative intensities in each band (shown in Figs. SI8 and SI9). The positions of the TPES and PES vibrational components agree to within 1 meV apart from the second component of the second band (band b) where the TPES value is higher than the PES value by 4 meV. This arises from contributions from autoionization from known I atom Rydberg states which move the band maximum to higher ionization energy (23). Bands a and b, the first two components of the second band of IF, contain contributions from I atoms. Band a is measured in the PE spectra as (11.244 ± 0.001) eV (with the I atom $I^+(^3P_0) \leftarrow$

$I(^2P_{3/2})$ band at 11.251 eV) and band b is measured in the PE spectra as $(11.329 \pm 0.001 \text{ eV})$ (with the I atom $I(^3P_1) \leftarrow I(^2P_{3/2})$ band at 11.330 eV). These contributions in bands a and b were not resolved in the TPE spectra, although for band a extra structure was observed on its higher energy side above 11.251 eV in the TPE spectrum associated with I atom Rydberg state autoionization resonances and, as stated above, for band b the TPES value is above the PES value because of I atom autoionization contributions (23).

Once the PE spectral envelopes for the two IF bands had been obtained, these envelopes were simulated using Franck-Condon calculations to obtain the ionic state bond length in each case. To do this, the spectroscopic constants ω_e , $\omega_e x_e$ and r_e for each electronic state are needed to generate Morse potentials for the IF and IF^+ states. Then the vibrational wavefunctions for each electronic state were obtained from numerical solutions of the vibrational Schrödinger equation with the appropriate Morse potential. The vibrational constants (ω_e , $\omega_e x_e$ and r_e) used for the $IF(X^1\Sigma^+)$ state for these simulations were taken from published sources, a rotational and vibrational analysis of an electronic emission spectrum and from a microwave spectroscopic study. The vibrational constants ω_e and $\omega_e x_e$ used for the ionic states were obtained by measuring the spacing (ΔE) between the IF vibrational components of each IF band in the PE spectrum. Since the equilibrium bond length of each ionic state is not known, trial values must be used in each case in the calculation of the Franck-Condon factors. These trial values were chosen to be close to, although shorter than, the value of the neutral state. This is because in both IF bands, an electron has been removed from an antibonding orbital; the equilibrium bond length of the ionic state is therefore expected to be shorter while the vibrational constant ω_e is expected to be larger than for the $IF(X^1\Sigma^+)$ state, as was observed. The actual equilibrium bond length of the ionic state is found by choosing a range of trial values and calculating the quantity $\Sigma[FCFv^+(\text{calc}) - FCFv^+(\text{expt})]^2$ for each trial bond length (10). A curve of this quantity plotted as a function of trial ionic bond length was then obtained. The lowest point of the curve represents the recommended value of the equilibrium bond length for the ionic state. During these FCF calculations, it was assumed that the electronic transition moment is constant over the photoelectron band. This leads to an error in the equilibrium bond length of the ionic state of $\pm 0.005 \text{ \AA}$ (10).

The values obtained for both IF bands are compared with the values obtained in the previous HeI PES work (71) in Table 3. It is notable that the Franck-Condon envelopes for the first two bands of IF are slightly different and the derived equilibrium bond lengths for the $X^2\Pi_{3/2}$ and $^2\Pi_{1/2}$ ionic states are also slightly different. As these ionic states both arise from the

IF $(7\pi)^{-1}$ ionization, their potential curves might be expected to have the same shape and their equilibrium bond lengths and harmonic vibrational constants might be expected to be the same. However, interaction between ionic states (notably spin-orbit interaction between the $^2\Pi_{1/2}$ ionic state and the $^2\Sigma^+_{1/2}$ ionic state arising from the $(13\sigma)^{-1}$ ionization) would lead to the $X^2\Pi_{3/2}$ and $^2\Pi_{1/2}$ ionic states having slightly different equilibrium constants and potential curves with slightly different shapes. This would explain why slightly different Franck-Condon envelopes are observed for the first two IF bands.

Table 3

This work has investigated IF bands in the ionization energy region 10.0-15.0 eV by PES. Their relative vibrational component intensities have been measured and, where IF and I bands are overlapped, their relative contributions have been established. Improved AIEs and VIEs of the $\text{IF}^+(X^2\Pi_{3/2}) \leftarrow \text{IF}(X^1\Sigma^+)$ and $\text{IF}^+(^2\Pi_{1/2}) \leftarrow \text{IF}(X^1\Sigma^+)$ ionizations and improved spectroscopic constants ω_e , $\omega_e x_e$ and r_e for the two IF ionic states $X^2\Pi_{3/2}$ and $^2\Pi_{1/2}$ have also been obtained. The extra structure seen in the TPE spectra, notably associated with bands (a) and (a'), and the position of band (b), which is higher in the TPE spectrum compared to its position in the PE spectrum by 4 meV, can be attributed to autoionization contributions from known I atom Rydberg states.

2.3 Angle resolved PES and CIS of atoms

O, S, N and I have been studied with the angle resolved PES and CIS methods using synchrotron radiation as the photon source (33-35,40,41). These are all reactive open shell atoms. Investigating their photoionization behaviour experimentally, which includes determining their angular distribution parameters and measurement of their partial photoionization cross-sections as a function of photon energy, provides valuable information which allows comparison between experiment and theory. Theoretical support for photoionization of open shell atoms and molecules is much less well developed than for closed shell systems and experimental studies on open shell systems should provide valuable information that can be used to encourage development of theoretical methods and test calculations. It is important to note that, unlike the closed shell case, removal of a single electron from an open shell system can give rise to several possible ionic states, which in the presence of the outgoing electron will give a number of final states. Careful treatment of these

final states, and their coupling, is necessary in a reliable theoretical model. The example chosen to illustrate the information to be obtained and the need for improved theoretical support is atomic iodine. It will be evident that current calculations of total and partial cross sections as a function of photon energy for atomic iodine are not good enough to allow a meaningful comparison with experimental CIS spectra. A similar situation applies to the experimental plots of angular distribution parameters as a function of photon energy although some insight into the photoionization dynamics can be obtained by applying the angular momentum transfer formulation of Dill (83) to the ionization processes considered.

2.3.1 Iodine atoms (40,41)

Iodine atoms were prepared using the method described above i.e. from the consecutive rapid reactions that occur on reacting F and CH₂I₂. As can be seen from Figures 12 and 13, the first and fourth (5p)⁻¹ bands of I atoms are not overlapped by IF features and they were therefore selected for CIS measurements. CIS spectra of these bands were recorded up to the fifth (5p)⁻¹ I atom ionization at 14.109 eV. The photon energy range used was 12.9 -14.1 eV. The asymmetry parameter, β , was measured for the first and fourth (5p)⁻¹ bands of iodine atoms over this photon energy range, at each photon energy, by recording CIS spectra at two angles (0° and 54° 44'), with respect to the direction of polarization of the photon source.

The β parameter was then calculated from the expression:-

$$\beta = R - 1 \quad \text{----- (6)}$$

where $R = \frac{I_0}{I_{54^\circ 44'}}$ is the ratio of the experimental intensities at the two angles used.

CIS Spectra

CIS spectra recorded for the two selected PE bands each show resonances which are parts of Rydberg series converging to the ¹S₀ ionic state. To assign the series, it is helpful to draw up a table (Table 4) of the excited Rydberg states to which transitions are allowed from the ground state ...5s²5p⁵(²P_{3/2}) and which autoionize to the ionic states I⁺..5s²5p⁴(³P₂) and I⁺..5s²5p⁴(¹D₂) respectively, in the J_cl coupling scheme. (This is also known as the JK coupling scheme; it has been shown to be most appropriate for describing neutral iodine Rydberg states (40)). In this coupling scheme, the total angular momentum of the ion core, J_c, couples with the orbital angular momentum of the Rydberg electron, l, to give K. The spin of the Rydberg electron, s, is then coupled to K to give the total angular momentum, J.

As already seen for SO in section 2.1, resonances seen in experimental CIS spectra often show an asymmetric profile. This is due to interference between the direct and indirect ionization processes and results in a characteristic Fano profile, where the cross section can be expressed as:-

$$\sigma(E) = \sigma_a \times \frac{(q + \varepsilon)^2}{1 + \varepsilon^2} + \sigma_b \quad (7)$$

In this equation, σ_a and σ_b represent two portions of the cross section which correspond, respectively, to transitions to states of the continuum that do and do not interact with the discrete autoionizing state. ε is the reduced energy which can be expressed as follows:

$$\varepsilon = \frac{E - E_n}{\frac{1}{2}\Gamma} \quad (8)$$

where E_n is the resonance energy and Γ is the natural width of the autoionizing state which represents the bound-continuum mixing of the resonance state. The parameter q characterises the line profile, and neglecting the background cross section, the resonance has a maximum at $\varepsilon_{\max}=1/q$ and is zero at $\varepsilon_0 = -q$. The sign of q thus determines whether the maximum occurs before or after the minimum. The magnitude of q indicates qualitatively the relative probabilities of the transition to the Rydberg state and direct ionization.

Codes for fitting resonances in the experimental CIS spectra to a convolution of the Fano profile and the instrumental function $F(E, \Omega)$, where Ω is the energy resolution measured by the full width at half maximum (FWHM), have been written, where the total cross section is expressed as:

$$\sigma(E, \Omega) = \int_{-\infty}^{\infty} \sigma(E_n - E) \cdot F(E, \Omega) dE \quad (9)$$

A Gaussian function was used as the instrumental function with an energy width of 3 meV, which is consistent with the photon width previously determined for CIS spectra recorded for oxygen atoms (33). Fano fitting of the resonances in this way allows the resonance positions, E_n , as well as the parameters q , and Γ to be established.

The effective quantum number ($n^* = n - \delta$) and principal quantum number (n) of each Rydberg state can then be determined from:-

$$E_n = E_\infty - \frac{R}{(n - \delta_n)^2} \quad (10)$$

where R is the Rydberg constant for iodine atoms, and E_n are the observed resonance energies of the Rydberg states. This equation can then be used, with known E_n and n values, to obtain the ionization energy, E_∞ and the quantum defect, δ_n of the series. This Fano fitting procedure follows closely that used previously to analyse CIS spectra of N and S atoms (35,38).

Table 4

Figures 14 (a) and (b) show CIS spectra of the $I^+(^3P_2) \leftarrow I(^2P_{3/2})$ PE band recorded in the photon energy region 12.9-14.1 eV at angles of 0° and $54^\circ 44'$ respectively with respect to the direction of polarization of the photon source. Corresponding spectra were obtained for the $I^+(^1D_2) \leftarrow I(^2P_{3/2})$ PE band (see Fig.SI10). These spectra show two clearly distinguishable Rydberg series converging to the $I^+(^1S_0)$ threshold, one which is broader than the other. This general pattern was observed in all CIS spectra recorded at 0° and $54^\circ 44'$ for these two PE bands in this photon energy region. The shapes of the resonances were slightly different for CIS spectra recorded for the first and fourth PE bands (see Figures 14 and SI10) while the resonances were similar in shape for CIS spectra recorded for the same PE band at the two different angles with respect to the photon beam polarization direction. According to Table 4, the same transitions are allowed from the ground state $I \dots 5s^2 5p^5(^2P_{3/2})$, to the excited states $I^* \dots 5s^2 5p^4(^1S_0) ns$ or nd , whether the ionic state after autoionization is the $I^+ \dots 5s^2 5p^4(^3P_2)$ or the $I^+ \dots 5s^2 5p^4(^1D_2)$ state. From this table, it can be seen that three series which converge to the $I^+(^1S_0)$ threshold are allowed, one ns and two nd series. Since only two series are observed and the quantum defects obtained for them correspond to the assignment of one ns and one nd series, it is assumed that the splitting between the two expected states, $nd[2]_{5/2,3/2}$, for a given n value is too small to be resolved in this work. Of the two observed series, the nd series is expected to be broader than the ns series, as has been observed in other halogens and rare gases, except for the atoms of the first row.

Table 5

From equation (10), the effective quantum number, n^* , and principal quantum number, n , were derived for each Rydberg state. The results obtained from the Fano fitting are shown in Table 5 (and Table SI3). Also included in these tables is the value of the product Γn^{*3} , the reduced linewidth. Table 5 presents the values obtained from resonances seen in the CIS spectrum of the first band, $I^+(^3P_2) \leftarrow I(^2P_{3/2})$ at $54^\circ 44'$, while the values obtained from the CIS spectrum of the fourth band, $I^+(^1D_2) \leftarrow I(^2P_{3/2})$ at $54^\circ 44'$ are shown in the Supplementary Information (Table SI3). Inspection of these tables shows that as n goes up, Γ , the linewidth, goes down as the Rydberg state lifetime goes up. Γn^{*3} is expected to be constant within a series (40,41). Also, the q value, the line profile index, is expected to show a smooth trend with increasing n . The agreement with the expected trends is only moderate although the errors in the values obtained are significant. Inspection of Table 5 (and Table SI3), and the corresponding results obtained at 0° , shows that the q values are negative for the $5s^25p^4(^1S_0)$ ns resonances seen in both the $I^+(^3P_2) \leftarrow I(^2P_{3/2})$ and $I^+(^1D_2) \leftarrow I(^2P_{3/2})$ CIS spectra recorded at 0° and $54^\circ 44'$ whereas for the $5s^25p^4(^1S_0)$ nd $[2]_{5/2,3/2}$ resonances the q values are positive for the $I^+(^3P_2) \leftarrow I(^2P_{3/2})$ channel and negative for the $I^+(^1D_2) \leftarrow I(^2P_{3/2})$ channel.

The position of the resonances, E_n , at the two angles and for the two different PE bands are in good agreement. From these values, the $I^+(^1S_0) \leftarrow I(^2P_{3/2})$ ionization threshold and the quantum defect can be obtained for each observed series using equation 10 (see Table 6). The derived $I^+(^1S_0) \leftarrow I(^2P_{3/2})$ ionization energies are in good agreement with the value obtained previously by photoabsorption measurements (99,100).

Table 6

Angular distribution parameters (β) vs photon energy

The Bethe-Cooper-Zare formula (101) can be used to assist interpretation of results of angular distribution experiments of light closed-shell atoms. However, this formula assumes L-S coupling in the initial and final states, neglects angular momentum exchange between the escaping electron and the ion core, and neglects configuration mixing in the initial and final

states. This approach is not expected to be appropriate for iodine, an element where configuration mixing and relaxation effects are important and where JK coupling is the most appropriate coupling scheme for excited states.

To obtain some guidance as to what might be expected for values of the angular distribution parameter, β , both on and off resonances, it is valuable to use angular momentum transfer theory (83) to investigate possible values of the β -parameter for parity favoured and unfavoured ionization channels. In this theory it is emphasized that photoionization can be accompanied by a transfer of angular momentum between the neutral atom and the final state (the atomic ion and the photoelectron). The photoionization process can be represented schematically as (83) :-

$$X(J_0\pi_0) + h\nu(j_{hv} = 1, \pi_{hv} = -1) \rightarrow X^+(J_c\pi_c) + e^- [l s j, \pi_e = (-1)^l] \text{ ----- (11)}$$

where $X(J_0\pi_0)$ and $X^+(J_c\pi_c)$ represent the atom and ion respectively, with total angular momentum J and parity π . (Parity of an atomic state is determined by $\sum l_i$ for that state. It is even for $\sum l_i$ even and odd for $\sum l_i$ odd).

The angular momentum transferred between the atom, and the ion and photoelectron, j_t , is defined by:

$$\vec{j}_t = \vec{j}_{hv} - \vec{l} = \vec{J}_c + \vec{s} - \vec{J}_o \text{ ----- (12)}$$

where $\vec{J}_0 + \vec{j}_{hv} = \vec{J}_c + \vec{s} + \vec{l}$

Conservation of parity, π , also implies

$$\pi_{hv} \times \pi_0 = \pi_c \times \pi_e \text{ ----- (13)}$$

which in the electric dipole approximation reduces to

$$\pi_c \times \pi_0 = (-1)^{l+1} \text{ ----- (14)}$$

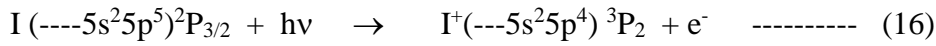
The parity transfer, π_t , is defined as the difference in parities between the neutral and ionic states. If π_t matches j_t (both odd or both even), then the ionization is parity favoured. When π_t and j_t are not matched (one odd, the other even), then the ionization is parity unfavoured and the asymmetry parameter, β_{unf} , is -1 .

Table 7 shows values of the asymmetry parameter, β , at different values of angular momentum transfer, j_t , obtained from the work of Dill and Fano (83,102) by Chang (103). In general, the asymmetry parameter is given as a weighted average of the possible $\beta(j_t)$ contributions as follows:-

$$\beta = \frac{1}{\sigma} \sum_{j_{cs}} \left(\sum_{j_t}^{\text{fav.}} \sigma(j_t)_{\text{fav}} \beta(j_t)_{\text{fav}} - \sum_{j_t}^{\text{unf.}} \sigma(j_t)_{\text{unf.}} \right) \quad \text{-----} \quad (15)$$

The results shown in Table 7 can be used to obtain values of $\beta(j_t)$ for specific ionization channels and thus help to understand the experimental β -plots.

If the case of direct ionization from the ground state of I to the ground state of I^+ is considered i.e.



then for this ionization, $\vec{j}_t = \vec{2} + \vec{1}/2 - \vec{3}/2$, which gives $j_t = 0, 1, 2, 3, 4$

Also π_t is odd, and as l must be even (as removal of a p electron in the atom will give an s or d free electron), $\pi_c \pi_o$ must be odd.

Inspection of Table 7, shows that when l is even, $j_t = 0$ is not possible.

Also, for

$j_t = 1, l = 0$ or 2 , and $\beta(j_t) = 0$ or 1 respectively

$j_t = 2, l = 2$, $\beta(j_t) = -1$, this channel is parity unfavoured

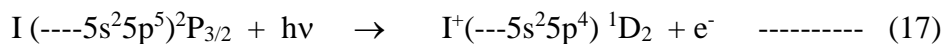
$j_t = 3, l = 2$ or 4 , $\beta(j_t) = 2/7$ or $5/7$ respectively

$j_t = 4, l = 4$, $\beta(j_t) = -1$ this channel is parity unfavoured

When j_t is odd, it matches the parity transfer π_t , which is also odd for the $5p^5 \rightarrow 5p^4 + e^-$ ionization.

In contrast, when j_t is even, the ionization channel is parity unfavoured and $\beta = -1$.

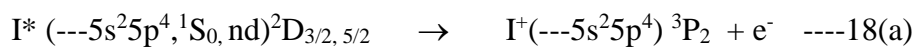
For direct ionization to the fourth state of I^+ ,



as the J quantum number of the ion is equal to 2 ($J_c = 2$) as in the above example

(equ.(16)), the results derived above for the first PE band of iodine atoms also apply to the fourth band. For non-resonant photon energies, the β -plots for these two bands will therefore be a weighted average of parity favoured and unfavoured partial cross-sections.

For resonant photon energies, the decay from the resonant state to the ionic state must also be considered e.g.



where in each case the resonant state is considered to be a member of a Rydberg series which converges to the $I^+---5s^25p^4\ ^1S_0$ ionic limit. These processes do not involve a photon and as a result equation (14) changes for these autoionizations to:-

$$\pi_c\pi_o = (-1)^l$$

The excited neutral states in equations 18(a) and (b) have $J = 1/2$ (from ns resonant states), $3/2$ and $5/2$ (from nd resonant states).

Taking as an example an autoionization from an excited state with $J=1/2$, then j_t between the excited atom I^* and the atomic ion including the spin of the photoelectron is $\vec{j}_t = \vec{2} + \vec{1}/2 - \vec{1}/2 = 1, 2, \text{ and } 3$

In this case, l is even, $\pi_c\pi_o$ is even, and π_t is even.

These j_t values (1,2 and 3) are already present in the direct ionization process. Autoionization via one of these channels will therefore enhance the roles of channels that are already present in direct ionization.

A similar situation also applies to autoionization from an excited state with $J = 3/2$.

Possible j_t values are 1,2,3 and 4 which are the same as those for direct ionization.

However, decay from an excited state with $J = 5/2$ will have

$$\vec{j}_t = \vec{2} + \vec{1}/2 - \vec{5}/2 = 0, 1, 2, 3, 4 \text{ and } 5$$

Again, l is even, $\pi_c\pi_o$ is even, and π_t is even.

These j_t values mean that there will be one new channel with $j_t = 5$.

The same analysis applies to the $I^+(-5s^25p^4)\ ^1D_2$ ionic state in equations 18(a) and (b) as the ionic state J value is 2 both for the 3P_2 and 1D_2 ionic states.

This analysis indicates that autoionization may enhance the contributions of some channels in direct ionization, and it can also give rise to extra channels, with new j_t values, which are not present in direct ionization. Also, it can be seen that j_t values of 1, 2 and 3 are obtained from $(---5s^25p^4, ^1S_0, ns)$ resonant sates and j_t values of 1, 2, 3, 4 and 5 are obtained from $(---5s^25p^4, ^1S_0, nd)$ resonant states.

Table 7

Figure 14

Figure 15(a) shows the β -plot of the first band of iodine atoms, $I^+(^3P_2) \leftarrow I(^2P_{3/2})$, and Figure 15(b) shows the β -plot of the fourth band of iodine atoms, $I^+(^1D_2) \leftarrow I(^2P_{3/2})$. The resonance positions in the CIS spectra have been marked on these figures for reference. These spectra are different from the CIS spectra as the resonances have similar shapes for the two bands and are symmetric. Also, the values of the beta parameter are different in Figure 15(a) and 15(b). Off resonance, the beta parameter for the first band of iodine atoms has a mean value of approximately -0.3. It shows a broad oscillating background with values changing from -0.4 and -0.10 and sharp resonances going to -0.5 (see Figure 15(a)). The beta parameter for the fourth band of iodine atoms has a mean value of -0.6 across the photon energy range with dips at the resonances going to -0.85. Comparison of Figures 14 and 15 (and Fig.SI10) shows that only the $nd[2]_{5/2,3/2}$ series is seen in the beta plots; the ns series is not seen. As outlined earlier, the beta parameter for iodine atoms at any photon energy for these two PE bands will be a weighted average of parity favoured and parity unfavoured ionization channels. In Figures 15(a) and 15 (b), the background is approximately -0.30 and -0.60 respectively, so both parity favoured (β zero or positive) and unfavoured channels ($\beta = -1$) are clearly playing a part (see Table 7).

The first resonance in Figure 15(a) has a minimum of -0.47 and a width of 22 meV. The second one has very similar characteristics with a minimum at -0.48 and a width of 21 meV. The higher resonances have a minimum of approximately -0.4 with widths decreasing from 15 meV to 7 meV. The resonances in Figure 15(b) decrease regularly in intensity, with a minimum of -0.90 and a width of 33 meV for the first resonance and a minimum of -0.65 with a width of 8 meV for the last observed resonance. The fact that the resonances are more negative than the general background level shows that the parity unfavoured channels are enhanced on resonance. This seems to be the case even more strongly for the β -parameter plot shown in Figure 15(b) where the resonances have minima close to -1.0.

Extensive angular distribution studies have been carried out on the outermost $(np)^{-1}$ ionizations of the inert gases Ne, Ar, Kr and Xe (82,104-106) in which the variation of β with photon energy has been compared with the variation of the cross-section. These studies showed that, in general, resonances are expected in the β -plots when resonances are observed in the CIS plots. The shape of the resonances in the β -plots can vary from one resonance to another, being symmetric or asymmetric. In most cases, the β parameter is positive, except at resonances, where β usually has a minimum below 0. Specifically, in xenon (104-106), which has one more electron than iodine and is closed shell, the nd and ns resonances are seen in both the CIS

and β -plots, with the nd resonances being broad and the ns resonances sharp, in both the CIS and β -plots. Comparing the β -plots of iodine and xenon, the nd resonances are seen in both iodine and xenon, but the ns resonances are not seen in iodine. This is probably due to an increase of the exit channels accessible in iodine arising from the increased coupling possibilities of the free electron with the ion in the case of the open shell iodine atom compared to xenon. Also, the fact that the β parameter is always negative in the present work, and becomes more negative on resonances, indicates that the parity unfavoured terms play a significant role with interference terms and interchannel coupling also probably contributing. As stated earlier, the j_t values of 1, 2 and 3 are expected from ($5s^25p^4, ^1S_0$, ns) resonant states and j_t values of 1, 2, 3, 4 and 5 are expected from ($5s^25p^4, ^1S_0$, nd) resonant states. As l , the angular momentum quantum number of the free electron, must be even, as removal of a p electron will give an s or d free electron, the values of $j_t = 1, 3$ and 5 correspond to parity favoured channels which have β values which are zero or positive. For $j_t = 2$ or 4, the channels are parity unfavoured and have $\beta = -1$ (see Table 7). As the β -plots in Figure 15, show only nd resonances, not ns resonances, with β values more negative than the negative background level, it appears that the $j_t = 4$ channel is the major contributor to the β values on resonance seen in Figure 15, as the $j_t = 2$ channel will be available for autoionization from the ns resonances.

Figure 15

These CIS and β -plots have been extended to higher photon energies, 11.0-23.0 eV for the first band, and 12.3-23.0 eV for the fourth PE band. They are structured up to 14.1 eV, the fifth I atom ionization energy, but show little structure above 14.1 eV.

In summary CIS spectra have been recorded for the first and fourth PE bands of atomic iodine, the $I^+(^3P_2) \leftarrow I(^2P_{3/2})$ and $I^+(^1D_2) \leftarrow I(^2P_{3/2})$ ionizations, in the photon energy range 12.9-14.1 eV. Resonances were observed in these spectra corresponding to excitation to Rydberg states which are parts of series which converge to the $I^+(^1S_0)$ ionization threshold. These were assigned to excitation to one ns and one nd series, although the observed nd series is thought to consist of two unresolved series, $nd_{5/2}$ and $nd_{3/2}$. Each Rydberg resonance was fitted to a Fano profile to determine the resonance position. The resonance positions were then fitted to obtain the ionization energies and quantum defects from the two series.

The β -plots show unexpected behaviour in that although resonances are seen in the β -plots at the same positions as the nd resonances in the CIS spectra, no resonances were observed in the β -plots at the positions of the ns resonances seen in the CIS spectra. Also, in these plots, β is negative off-resonance and becomes more negative on-resonance. This is in contrast to the equivalent β -plots for xenon and the lighter halogen atoms, notably bromine, which show resonances in the same positions as the resonances in the CIS spectra, and which have positive values off-resonance and are negative on-resonance. It appears that parity unfavoured channels are playing a greater role in iodine than in bromine or xenon. At non-resonant photon energies, the $j_t = 2$ and $j_t = 4$ channels make significant contributions whereas at photon energies at nd resonant positions, the $j_t = 4$ channel dominates.

Improved calculations of total and partial cross sections and angular distribution parameters of atomic iodine as a function of photon energy are required as agreement between experimental and theoretical results is at present relatively poor (107-109). For example, in theoretical studies (108,109) that have calculated the β parameter as a function of photon energy, β was computed to be always positive at different photon energies and to vary smoothly as a function of photon energy. However, both these studies used the independent particle approximation and did not take into account the contributions from resonant states. The demands on any theoretical method to reproduce the experimental results are clearly quite high. A suitable method must include interchannel coupling and other electron correlation terms, the effects of resonant states as well as relativistic effects. However, such calculations will be rewarding in that they should lead to greater insight into the photoionization behaviour of heavy open-shell atoms such as iodine.

3. Future Research

Studying reactive intermediates with PEPICO and TPEPICO

It is clear from the examples that have been presented that the study of a reactive intermediate by PES can suffer from a problem in that a PE band of a reactive intermediate may be overlapped by one or more bands from the precursor, reactant or product molecule(s) and/or secondary products. For example, this is seen in the partial overlap of SO bands with bands of SO₂, when SO is prepared by discharging flowing SO₂, and the partial overlap of I and IF bands from the F + CH₂I₂ reaction. This problem could be avoided by using the photoelectron-photoion coincidence (PEPICO) or the threshold photoelectron-photoion coincidence (TPEPICO) methods.

In PEPICO and TPEPICO, the photoelectron and photoion formed in a single ionization event are detected in a spectrometer which has both a photoelectron energy analyser and ion mass analyser (110,111). Photoelectrons and photoions are extracted in opposite directions by an applied electric field. The energy of the photoelectrons can be selected and the mass of the corresponding photoion determined. This is achieved by measuring the flight times of the electrons and ions to the detectors on the photoelectron and mass analysers respectively. The electron and ion from one photoionization event arrive at their respective detectors at different times after their formation and although the signals at the detectors are not really “coincident”, they do have a definite temporal relationship. As electron flight-times are much smaller than the flight times of the corresponding ions, the detected electron signal is used as the start pulse and the ion signal provides the stop pulse allowing signals from the same event to be detected “in coincidence”. In this way the PEPICO and TPEPICO methods measure time-correlated electron-ion pairs produced on photoionization. This approach can be extended to the study of dissociative photoionization where photoelectron and fragment cations are detected in coincidence.

The difference between the PEPICO and TPEPICO methods is that in PEPICO the photon energy used for ionization is fixed, usually well above the ionization energy of the molecule of interest, and the energy of the photoelectrons detected is chosen to select an electronic (and vibrational) state of the photoion, whereas in TPEPICO only threshold photoelectrons are detected and the photon energy is scanned to select different electronic (and vibrational) states of the cation. In both methods, each detected photoelectron can be registered in coincidence with the corresponding ion. This provides a PE or TPE spectrum for each mass, which could be used, for example, as a fingerprint for identifying and quantifying isomers in a reactive environment, such as a flame, or, more generally, for obtaining a PE or TPE spectrum of a reactive intermediate in a reaction system.

One of the major experimental problems in TPEPICO studies has been the simultaneous optimization of the electron energy resolution and the ion time-of-flight (TOF) mass resolution. Good electron resolution requires low extraction fields, whereas good ion TOF mass resolution requires high extraction fields. One approach around this problem has been to use low extraction fields for electron energy resolution, and then once an energy selected electron is detected, the associated ions are extracted with a large pulsed electric field. However, such pulsed ion extraction impedes the accurate determination of ion dissociation rates from the ion TOF distribution. It also results in a false coincidence signal that is sometimes difficult to distinguish from the true coincidence signal. Baer and coworkers addressed this problem in

two stages (112). First, by using velocity map imaging (VMI) in TPEPICO experiments, they demonstrated a significant improvement in collection efficiency and energy resolution of threshold electrons. This permitted focussing electrons from a relatively large photoionization region, as occurs in synchrotron experiments, to a small spot on a detector. The collection efficiency of ions was demonstrated to be good and the ion/electron resolution problem was improved with this VMI approach. However, this improvement still suffered from “hot electrons” contributing to the TPE spectrum because the velocity focussing optics used focus both energetic and slow electrons to a small spot on the detector as long as their velocities in the direction of the detector are the same. Baer and coworkers addressed this second problem by using the VMI velocity focussing optics to suppress the effects of “hot electrons”(113). This was done by monitoring the electrons both at the centre of the detector (threshold electrons and those energetic electrons with initial velocity vectors along the direction to the detector) and electrons at a selected position off-axis (energetic electrons with perpendicular velocity components). The TPE signal was then derived by subtraction of the off-axis signal from the signal at the centre of the detector. (More generally, a subtraction/renormalisation procedure is used (114)). However, this subtraction approach can lead to imperfect subtraction of energetic electrons or the introduction of artefacts. A better way to separate energetic and threshold electrons is to use Abel inversion and reconstruction of the compressed 2D image on the detector using appropriate software (e.g. ref. 115). This method (116) has the added advantage that CIS plots can be obtained and β -parameters can be recorded as a function of photon energy (117,118). These subtraction methods, using the VMI technique, have the great advantage of operating in a fully continuous mode, which are well adapted to a synchrotron source operated in multibunch mode and for which application of TPEPICO is straightforward.

TPEPICO methods have been applied at several synchrotron facilities to determine ionization energies of reactive intermediates and heats of formation of their ions (Table 2, 58,114-122), as well as dissociation limits and ionic appearance energies, kinetic energy releases (KERs) and fragmentation breakdown diagrams of state-selected ions (123,124). They have also been used to investigate bimolecular ion-neutral reactivity (125) and the fragmentation dynamics of ions produced by photoionization (21).

Three important advances have expanded the power of PEPICO and TPEPICO and permitted their implementation with modern synchrotron radiation (111).

(i)As discussed above, the use of velocity focussing of threshold electrons onto an imaging detector has improved the sensitivity and electron energy resolution, and also facilitated the

subtraction of the energetic electron background. An important advantage of VMI-based imaging electron analyzers lies in their inherent high collection efficiency (collection over 4π steradians) allowing a natural and optimum coupling with ion detection. This is very important for PEPICO and TPEPICO studies of reactive intermediates. Coincidence studies of this type are not really feasible with electrostatic electron analysers, such as hemispherical analysers, as used in the PE, CIS and TPE studies described in section 2, because of their poor collection efficiency which is not compatible with a typical rate of false coincidences.

(ii) The development of multi-start multi-stop collection detectors for both electrons and ions has permitted the use of the full intensity of modern synchrotrons thereby greatly improving signal-to-noise ratios. A straightforward multi-start multi-stop procedure has been developed that ensures the highest signal-to-noise, constant background that can easily be removed, and fast data acquisition (126).

(iii) Finally, recent experimental improvements involving imaging electrons of a range of energies as well as ions onto separate position-sensitive detectors has further enhanced the collection sensitivity. Notably, it has been shown (127) that the false-coincidence barrier, which limits the dynamic range (the ability to detect a small signal in the presence of a much larger background signal) of conventional PEPICO and TPEPICO experiments, can be overcome by using ion imaging with a rapidly modulated electric deflection field acting on the ion trajectories at a fixed fraction of their flight time. This improvement of the dynamic range is particularly significant for studies of reactive intermediates when the electron and ion signals for the reactive intermediate of interest are much lower than those of the stable molecules present, as is often the case.

With the older technique of PIMS, the study of atoms and molecules (reactants, intermediates and products) in flames using tunable vacuum ultraviolet radiation from a synchrotron source is well established (128-131). However, although isomers can be detected and studied with this approach, the method has some limitations (132-134). Isomer identification and quantification is possible with this method because the isomers will have different AIEs. For each isomer, parent ion intensities need to be monitored as the photon energy is swept from just below the AIE to just above it. Therefore, a series of scans are required for each ion mass for a detailed analysis of flame chemistry. Isomer identification in these scans relies on information such as known photoionization efficiency (PIE) curves and ionization cross-sections, as well as computed AIEs and ionic and neutral potential surfaces for the neutral and ion, and computed Franck-Condon factors for the lower PE bands of each

isomer. Although, in principal, there is no limit on the size and number of isomers that can be identified by this approach, identification becomes difficult when the isomers have very similar AIEs, when there are three or more isomers present, and when the number of atoms in the isomers becomes moderately large (e.g. when there are more than four carbon atoms in isomers of a hydrocarbon molecule). PEPICO and TPEPICO offer a solution to this problem in that they provide a sensitive and selective way to identify and monitor isomers in flames, as the vibrationally resolved PE band of an isomer provides a unique fingerprint which leads to identification by comparison with literature spectra or spectra computed via electronic structure/Franck-Condon Factor calculations. This opens the door for future studies on the mechanism and kinetics of reactions in flames and plasmas. For example, in a study of hydrogen flames doped with different alkanes and alkenes with TPEPICO, hydrogen abstraction ratios from a number of alkanes and alkenes to form isomeric radicals were determined (135). In this work, it was found that for an n-butane doped flame TPE bands of 2-butyl and 1-butyl radicals were observed whereas for an i-butane doped flame TPE bands of t-butyl and i-butyl radicals were recorded. In each case, these radicals are expected from direct hydrogen-abstraction from the parent molecule. The results show that, for the alkanes and alkenes investigated, direct hydrogen abstraction, without rearrangement, is the major reaction pathway for the formation of fuel radicals in the hydrogen-rich flames investigated.

The TPEPICO and PEPICO modes of operation have been compared in a study of a number of reactive intermediates in a fuel-rich premixed, low pressure flame (136). TPEPICO has higher electron energy resolution than PEPICO but requires significantly longer measurement time. PEPICO, therefore, has a multiplex advantage over TPEPICO. However, TPEPICO is the better approach for obtaining well-resolved photoelectron spectra of reactive intermediates, although, as already discussed, the TPE vibrational band envelopes obtained may be affected by autoionization. Also, PEPICO is more appropriate for studying chemical reactions where species (including isomer) identification needs to be performed relatively quickly as a function of time (136). It is expected, therefore, that the multiplexing fixed photon energy PEPICO method will contribute effectively to the study of the reactivity and kinetics of reactive intermediates in flames and other environments and, as demonstrated by some recent examples, this is already proving to be the case (136-140). PEPICO can also provide further information such as photoelectron angular distributions and cation translational energies. The ion kinetic energy can be used to distinguish between a parent (translationally cold) and a fragment (hot) ion, which, for soft ionization, is extremely helpful to identify the ionized molecule (141).

In Table 2, a list of reactive intermediates studied by PEPICO and TPEPICO with synchrotron radiation is presented. Most of these studies were made at vuv beamlines at the SOLEIL synchrotron (France) or the Swiss Light Source. Also included in this table are references to earlier studies by conventional PES, where available. For convenience, only reactive intermediates with up to four atoms are considered in order that Table 2 is comparable with Table 1. The reactive intermediate photoelectron studies listed in Table 2 were all made with mass selected PE, TPE and SPE spectroscopy. Slow photoelectron spectroscopy (SPES) is similar to TPE spectroscopy but it provides more intensity for a given resolution (53,116). In Table 1, the methods used to make the reactive intermediates listed are microwave discharge of a flowing mixture of a precursor molecule diluted in an inert gas or fluorine atom abstraction from a target molecule in a flow-tube under effusive flow conditions. Flash-pyrolysis has also been used by other workers to generate reactive intermediates for spectroscopic study with synchrotron radiation (e.g. allyl (142) and propargyl and bromopropargyl radicals (143)). These methods have also been used to make the reactive intermediates listed in Table 2. For example, in ref.(45), the $F + H_2O$ reaction was used to make OH, and O atoms were made via the secondary reaction $F + OH$. Similarly, the $F + CH_4$ reaction, and subsequent H-abstractions, were used to make CH_2 (61) and CH (46), and C_2H was made in this reaction system via secondary reactions, notably $CH + CH \rightarrow C_2H + H$ (51). Fluorine atom abstraction from a suitable precursor has also been used to prepare NH(48), NH_2 (54), CN(47), CNC(52), CCN(52), CHCN(52), HBBH(59), and HNC(60). Pyrolysis methods have been used, with PN(49), PO(50), CF_3 (56), CH_2Br (57) and CH_3 (55) all being prepared by flash pyrolysis of suitable precursors, and CH_2I has been made by laser photolysis of CH_2I_2 (58). TPE spectra have also been obtained for O, H and OH from a stoichiometric acetylene flame by coupling a flat-flame burner with a flame-sampling molecular beam (44)

Comparison of the results of the two types of study (TPEPICO, PEPICO vs PES) shows the value of having information from both sources. For example, in the case of PO only the first band is observed in both cases and good agreement was obtained between the two types of spectra, with the measured AIE and the vibrational separations in the first band being the same within experimental error (77,50). In the case of PN, three vibrationally resolved bands were observed in the PES study (76) whereas only the first band was seen in the TPEPICO work (49). The AIE values of the first band were the same but the separation of the two vibrational components in the first band were different (1230 cm^{-1} in the PES work (76) ; 1320 cm^{-1} in the TPEPICO study (49)). Further TPEPICO measurements on PN would therefore be

valuable to obtain a reliable value for this separation and record the higher bands for comparison with the PES results. For CH₂Br and CH₂I, comparison of the TPEPICO spectra with the earlier PE spectra shows some interesting differences. In both cases only the first band of each radical has been observed and, as expected, the TPEPICO spectrum is better resolved than the PE spectrum. For CH₂Br, the TPEPICO spectrum (57) shows three regularly spaced vibrational components with the first component the most intense. The vibrational structure is assigned to excitation of the C-Br stretching mode in the ionic state. In the PE spectrum (79), four regularly spaced vibrational components are observed and the structure is again assigned to excitation of the C-Br stretching mode in the ion. The position of the first vibrational component, the AIE, agrees well with the TPEPICO value but the overall vibrational envelope is different with the second component being the most intense. This suggests that autoionization is affecting the vibrational envelope in the TPEPICO case causing an enhancement of the lowest vibrational component. However, the TPE band envelope is reproduced quite well by Franck-Condon factor calculations which use DFT derived potentials for the molecule and ion suggesting that the PE first band envelope should also be re-investigated experimentally. For CH₂I, again the TPEPICO spectrum (58) is better resolved than the PE spectrum (79) which shows a broad unstructured band. The TPEPICO spectrum has five regularly spaced vibrational components, which are assigned to excitation of the C-I stretching mode in the ionic state with the second component being the most intense.

For NH₂, the AIEs to the first two PE bands have been determined and the nature of the vibronic structure in each PE band has been investigated via a series of experiments involving PES, TPEPICO and pulsed-field-ionization zero-kinetic energy (PFI-ZEKE) PE spectroscopy (75,54,144,145). NH₂ and NH₂⁺ are prototypical triatomic hydrides which are subject to the Renner-Teller effect in some of their electronic states. The outermost electronic configuration of NH₂ in its ground state is -----3a₁²1b₁¹, where the half-filled 1b₁ molecular orbital consists of a nitrogen non-bonding 2p orbital perpendicular to the NH₂ plane, whereas the 3a₁ molecular orbital is H-H bonding and slightly N-H antibonding. The (1b₁)⁻¹ ionization gives rise to a ¹A₁ state, whereas the (3a₁)⁻¹ ionization gives ³B₁ and ¹B₁ states, and the energy order of these states is known from electronic structure calculations as ³B₁ < ¹A₁ < ¹B₁ (i.e. the \tilde{X} , \tilde{a} and \tilde{b} states). While the equilibrium bond lengths in these states do not differ significantly from those of the \tilde{X}^2B_1 neutral state, the equilibrium bond angles do show significant differences. The \tilde{a}^1A_1 ionic state has a similar equilibrium bond angle to the neutral \tilde{X}^2B_1 state whereas the \tilde{X}^3B_1 and \tilde{b}^1B_1 ionic states have significantly larger angles. Hence, low

vibrational levels of the \tilde{a}^1A_1 NH_2^+ state can be accessed efficiently from the lowest vibrational state of the ground neutral state (the Franck-Condon factors are favourable) but low vibrational levels of the \tilde{X}^3B_1 and \tilde{b}^1B_1 NH_2^+ states cannot be accessed efficiently from the lowest vibrational level of NH_2 \tilde{X}^2B_1 (the Franck-Condon factors are unfavourable). However, low vibrational levels of the \tilde{X}^3B_1 and \tilde{b}^1B_1 NH_2^+ states have significant Franck-Condon factors with, and can be easily accessed from, the first excited state of the neutral, the NH_2 \tilde{A} state, which has a similar equilibrium bond angle to those of the \tilde{X}^3B_1 and \tilde{b}^1B_1 ionic states. In the PES study of NH_2 (75), the three bands corresponding to ionization from the \tilde{X}^2B_1 neutral state to the \tilde{X}^3B_1 , \tilde{a}^1A_1 and \tilde{b}^1B_1 ionic states were observed. The first and third bands were very broad, both showing a regular series in the NH_2 deformation mode in the ion, whereas the second band showed three components with the AIE component the strongest. The vibrational separations in this second band were assigned to excitation of the NH_2 deformation mode and the NH_2 symmetric stretching mode in the ion. For the first and third bands, the AIEs could not be reliably determined because of very poor Franck-Condon factors in the low ionization region of each band. After the PES study, which measured the second AIE as (12.45 ± 0.01) eV, the second AIE was improved to (12.43633 ± 0.00010) eV by a PFI-ZEKE PE study using xuv laser-derived radiation (144). Then by exciting to the \tilde{A} state of NH_2 and performing PFI-ZEKE measurements on selected rotational levels of the lowest vibrational level of this state, a value for the first AIE was obtained as (11.1689 ± 0.0001) eV (145). In the later TPEPICO study of NH_2 (54), the second band showed a very similar envelope to that recorded in the PES study with the first vibrational component the most intense. Its position, the AIE, was measured as (12.435 ± 0.002) eV in good agreement with the PES (75) and PFI-ZEKE values (144). For the first band, a broad envelope is observed with low intensity in the adiabatic region. Nevertheless, a weak vibrational component was observed at (11.170 ± 0.002) eV consistent with the PFI-ZEKE value for the first AIE (145).

As mentioned in the Introduction, absolute photoionization cross-sections of reactive intermediates are needed to convert experimental photoelectron band intensities into partial pressures. This is very important information which is, for example, needed to compare experimental partial pressures with those obtained from modelling the environments in which reactive intermediates play key roles. However, absolute photoionization cross-sections of reactive intermediates are difficult to obtain. Nevertheless, there have been some experiments reported recently which make a start in providing some of this vital information, with cross-

sections reported for $\text{Cl}_2\text{S}(\text{CH}_3)_2$ (2), OH (146,147), CH_3 (148), C_2H_5 (149), and C_4H_5 (2-butyn-1-yl) (150).

In a study of the atmospherically important reaction between dimethyl sulphide (DMS) and molecular chlorine (2), which proceeds via the intermediate $\text{Cl}_2\text{S}(\text{CH}_3)_2$:-



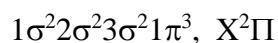
the photoionization cross-section of the first PE band of the intermediate was determined at 21.22 eV. This was achieved by first determining the absolute photoionization cross-sections of the first bands of the reagents (CH_3SCH_3 , Cl_2) and products (CH_3SCH_2 , HCl) in separate experiments which measured the first band intensities relative to the intensity of the first band of argon, which has a well established cross-section, at known partial pressures, and then, by recording photoelectron spectra of the reaction, which shows bands of the reagents, intermediate and products, at different reaction times.

In the case of the OH radical, there have been two measurements of the photoionization cross-section at vuv photon energies, derived from a synchrotron source (146,147). In both cases, cross-sections were measured at photon energies which are above the first AIE but below the second AIE. In the first study (146), OH was produced via the $\text{O}(^1\text{D}) + \text{H}_2\text{O}$ reaction in a flow reactor, where $\text{O}(^1\text{D})$ was obtained by photodissociation of O_3 . Partial pressures of OH were determined by fitting the observed time traces of the OH^+ signal, produced by vuv ionization of OH, with a kinetics model constructed using available rate coefficients. Photoionization cross-sections values were reported at 13.435 and 14.193 eV (146). In the second study (147), which is simpler and more direct, OH was produced from the $\text{F} + \text{H}_2\text{O}$ reaction, where fluorine atoms were produced by microwave discharge of a flowing F_2/He mixture, and the OH absolute cross-section was measured at 13.8 eV. This was achieved by measuring the photon intensities of H_2O^+ , OH^+ and O^+ at 13.8 eV with the microwave discharge on and off. By using the observed changes in ion signals, with the known cross-sections of O and H_2O at 13.8 eV, the cross-section of OH at this photon energy could be determined. Also, the OH^+ photoion intensity was recorded over the photon energy range 12.6-15.0 eV and the photoion intensity scale was converted to absolute photoionization cross-section using the measured value at 13.8 eV. The curve obtained shows good agreement with the CIS spectrum recorded for the $\text{OH}^+ \text{X}^3\Sigma, v^+ = 0 \leftarrow \text{OH X}^2\Pi, v^+ = 0$ ionization (30). Also, comparison of the cross-sections derived at 13.436 and 14.193 eV from this plot with those obtained earlier at these photon energies (146), shows that the earlier values are lower by approximately a factor of 2 indicating that further measurements are needed to resolve this

discrepancy. These examples highlight the point that the available experimental photoionization cross-sections of reactive intermediates have been measured relative to a suitable reference (or references, O and H₂O in the case of OH) with a known cross-section, such as a reagent or another reactive intermediate. For example, in the measurement of the absolute photoionization cross-section of the 2-butyne-1-yl radical (CH₃-C≡C-CH₂), at a photon energy just above its first ionization energy (150), the radical was obtained from the F + 2-butyne reaction and its cross-section was determined using the known cross-section of 2-butyne. Also, where comparison can be made between available calculated and experimental cross-sections, the agreement is poor (146,147,150), highlighting the need for improved methods to calculate cross-sections which include resonant excitation processes, particularly at low photon energies just above the first ionization threshold, as well as more cross-section measurements on reactive intermediates.

The information summarised in sections 1, 2 and 3 suggest that it would be very beneficial to carry out angle resolved PE and CIS studies with PEPICO. A recent study of the OH radical by PEPICO (45), using synchrotron radiation as the photon source, illustrates the advantages of combining information from these methods to obtain enhanced information on the ionic states accessed and the ionization processes.

The ground electronic state configuration of OH is



where each 1π orbital consists of an O $2p_\pi$ atomic orbital and is thus non-bonding in character, and the 3σ orbital is a bonding orbital consisting of H1s and O $2p_\sigma$ contributions. The $(1\pi)^{-1}$ ionization produces the $X^3\Sigma^-$, $a^1\Delta$ and $b^1\Sigma^+$ ionic states, while the $(3\sigma)^{-1}$ ionization gives rise to the $A^3\Pi$ and $c^1\Pi$ states. The 21.22 eV PE spectrum of OH shows all three bands associated with the $(1\pi)^{-1}$ ionization. They exhibit non-bonding envelopes with AIEs of 13.01, 15.17 and 16.61 eV. For the $(3\sigma)^{-1}$ ionization, only the $\text{OH}^+(A^3\Pi) \leftarrow \text{OH}(X^2\Pi)$ band has been observed. This is broad (AIE= 16.48 eV) with vibrational separations smaller than in the ground state neutral (66).

In ref. (45), a PEPICO spectrum of the first band of OH recorded at a photon energy of 15.00 eV is compared with that recorded at 21.22 eV. The 21.22 eV PE spectrum of the first band shows a strong adiabatic component and a weaker $v^+ = 1$ component (~ 10% of the $v^+ = 0$ component in intensity) (65,66). In contrast, the 15.00 eV PE spectrum observed in the PEPICO study shows enhanced intensity in the $v^+ = 1, 2$ and 3 components, relative to the $v^+ = 0$ component, with weaker intensity seen for $v^+ > 3$ components. The CIS study (30) shows

that this change in overall vibrational envelope derives from autoionization arising from resonance at 15.00 eV with one or more OH Rydberg states, which are lifetime broadened because of rapid autoionization. The dominant Rydberg state was identified as OH ($a^1\Delta, 9d$) with a possible contribution from OH($A^3\Pi, 3d$) (30). A similar enhancement in the $v^+ = 1, 2$ and 3 components, relative to the $v^+ = 0$ component, was observed in the case of OD at 15.0 eV photon energy and this could also be attributed to autoionization from resonant Rydberg states with OH⁺ ($a^1\Delta$) and OH⁺($A^3\Pi$) ionic cores.

This PEPICO investigation (45), and the studies reviewed in section 3, suggests that it would be very advantageous to use PEPICO, performed with a VMI analyser for electrons rather than a hemispherical electrostatic energy analyser as used in the work described in section 2, to make angle resolved PE and CIS measurements on reactive intermediates. Such studies are perfectly feasible but few PE and CIS studies of this type have yet been published. These should be extremely informative as, as described earlier (in sections 1 and 2), photoelectron angular distribution measurements provide information on the nature of the molecular orbital from which an electron has been removed and the angular momentum character of the free electron. Also, when autoionization occurs, the nature of the excited state can be investigated by angularly resolved PE and CIS studies. It is noted that for some of the reactive intermediates listed in Table 2, experimental information includes PE spectra recorded as a function of photon energy (this would form the basis of a CIS study) and β -parameters have been measured for the first bands of CF₃ (56) and HNC (60) at selected photon energies. However, much more progress in this area can be anticipated.

4. Conclusions

In this review, the development of photoionization studies of reactive intermediates with synchrotron radiation has been outlined by considering a number of examples. This research area developed from the study of reactive intermediates with conventional PES using an inert gas discharge as the ionization source, through to the present, where reactive intermediates are studied with PEPICO and TPEPICO using synchrotron radiation. Sections 1 and 2 have discussed the basic principles of PES, CIS and TPES and their application to study photoionization of reactive intermediates. Section 3 has outlined the basic principles of PEPICO and TPEPICO. It has also summarised recent studies and existing applications of

PEPICO and TPEPICO, and indicated areas of future application for the study of reactive intermediates, notably the use of PEPICO for angle resolved PES and CIS studies.

Acknowledgements

I would like to thank all members of the Southampton group and other colleagues who have collaborated with this research. I am particularly indebted to Dr Edmond Lee and Dr Alan Morris with whom I have worked for a significant period of time. Ed has been responsible for most of the supporting theory and calculations, and Alan has designed and built all of the spectrometers used. It is unfortunate that most of their work has not been discussed in this review, but their contributions have underpinned the research and been essential to its success.

Table 1

List of Studies of Reactive Intermediates with Synchrotron Radiation performed by the Southampton group

| Ref. No. | Topic | Technique/Synchrotron/Beamline(BL) | Earlier Conventional PES |
|----------|--|---|--------------------------|
| 26. | SO | PES, CIS Daresbury BL3.2 | 62 |
| 27. | SO | PES, CIS Daresbury BL3.2 | 62 |
| 28. | CS | PES, CIS Daresbury BL3.2 | 63 |
| 29. | O ₂ (¹ Δ _g) | PES, CIS Daresbury BL3.2 | 64 |
| 25. | PE Spectrometer | Description of the design and operation of the spectrometer | |
| 30. | OH, OD | PES, CIS Daresbury BL3.2 | 65,66 |
| 24. | A review | Summary of measurements made at Daresbury on BL3.2 | |

| | | | |
|-----|---|---|----------|
| 31. | O ₂ (¹ Δ _g) angle resolved study | PES, CIS Daresbury BL3.2 | 64 |
| 32. | Short over-view | A short over-view article of work to-date | |
| 33. | O atoms | PES, CIS Daresbury BL3.2 and Elettra BL4.2R | 67 |
| 34. | S, SH | PES at Elettra BL4.2R | 68 |
| 35. | N, OH | PES and CIS at Elettra BL4.2R | 65,66,67 |
| 36. | NO | PES and CIS at Elettra BL4.2R | 69 |
| 37. | CF | PES and CIS at Elettra BL4.2R | 70 |
| 38. | S | PES and CIS at Elettra BL4.2R | 68 |
| 23. | I, IF | PES and TPES at Elettra BL4.2R | 71 |
| 39. | CF ₂ | PES and TPES at Elettra BL4.2R | 13 |
| 40. | I | PES and CIS at Elettra BL4.2R | 71,72 |
| 41. | I | PES and CIS at Elettra BL4.2R | 71,72 |
| 42. | N ₂ Vibrationally excited | PES and TPES at Elettra BL4.2R | 73 |
| 43. | H ₂ O ₂ | PES and TPES at Elettra BL4.2R | 74 |

Table 2
List of Studies of Reactive Intermediates by PEPICO and TPEPICO with Synchrotron Radiation ^(a)

| Reactive Intermediate; No of Atoms n | Reference | PE Technique | Synchrotron ^(b) | Ref. to earlier Conventional PES |
|---|-----------|--------------|----------------------------|----------------------------------|
| n=1 | | | | |
| H | 44 | TPES | SW | 67,73 |
| O | 44,45 | TPES ,PES | SW, SL | 67 |
| | | | | |
| n=2 OH, OD | 44,45 | TPES,PES | SW, SL | 65,66 |
| CH | 46 | TPES,SPES | SL | |
| CN | 47 | SPES | SL | |
| NH | 48 | TPES,SPES | SL | 75 |
| PN | 49 | TPES | SW | 76 |
| PO | 50 | TPES | SW | 77 |
| | | | | |
| n=3 | | | | |
| C ₂ H | 51 | SPES | SL | |
| CNC | 52 | PES | SL | |
| CCN | 52 | SPES | SL | |

| | | | | |
|--|----|------|--------|----|
| C ₃ | 53 | SPES | SL | |
| CH ₂ | 61 | TPES | SL | |
| NH ₂ | 54 | TPES | SL, SW | 75 |
| HNC | 60 | PES | SL | |
| | | | | |
| n=4 | | | | |
| l-C ₃ H, c-C ₃ H | 53 | SPES | SL | |
| CH ₃ , CH ₂ D, CHD ₂ , CD ₃ | 55 | TPES | SL | 77 |
| CF ₃ | 56 | TPES | SL | |
| CH ₂ Br | 57 | TPES | SW | 79 |
| CH ₂ I | 58 | TPES | SW | 79 |
| HCCN | 52 | SPES | SL | |
| HBBH | 59 | SPES | SL | |

(a) Only Reactive Intermediates with up to 4 atoms are considered, in order that Table 2 is comparable with Table 1.

(b) SW = vuv beamline at the Swiss Light Source (Villigen, Switzerland)

SL = vuv beamline at the SOLEIL synchrotron (St.Aubin, France)

Table 3 Ionic vibrational constants and adiabatic and vertical ionization energies for the two observed IF bands.

| | IF ⁺ (X ² Π _{3/2}) | IF ⁺ (² Π _{1/2}) | IF ⁺ (X ² Π _{3/2}) ref. 71 | IF ⁺ (² Π _{1/2}) ref. 71 |
|---|--|---|---|--|
| ω _e [cm ⁻¹] | 696 ± 2 | 687 ± 2 | 700 ± 30 | 710 ± 30 |
| ω _e x _e [cm ⁻¹] | 3.0 ± 0.5 | 1.2 ± 0.5 | 10 ± 5 | 10 ± 5 |
| r _e [Å] | 1.836 ± 0.005 | 1.832 ± 0.005 | 1.82 ± 0.01 | 1.82 ± 0.01 |
| AIE [eV] | 10.538 ± 0.001 | 11.244 ± 0.001 | 10.54 ± 0.01 | 11.24 ± 0.01 |
| VIE [eV] | 10.538 ± 0.001 | 11.329 ± 0.001 | 10.62 ± 0.01 | 11.32 ± 0.01 |

Spin-orbit
Splitting [cm^{-1}]

5690 ± 8

5560 ± 40

Table 4

Allowed Rydberg states, which converge to the $\text{I}^+ 1\text{S}_0$ ionic state, to which transitions are allowed from the ground state $\text{I} \dots 5s^2 5p^5 ({}^2\text{P}_{3/2})$ and which autoionize to the ionic states $\text{I}^+ \dots 5s^2 5p^4 ({}^3\text{P}_2)$ or $\text{I}^+ \dots 5s^2 5p^4 ({}^1\text{D}_2)$, in the J_{cl} coupling scheme

| <i>Excited states</i> | $[J_{cl}]_{J_{final}}$ | <i>ionic state after autoionization</i> $\text{I}^+ {}^3\text{P}_2$ | <i>ionic state after autoionization</i> $\text{I}^+ {}^1\text{D}_2$ |
|--|------------------------|--|--|
| $5s^2 5p^4 ({}^1\text{S}_0) ns {}^2\text{S}_{1/2}$ | $[00]_{1/2}$ | $5s^2 5p^4 ({}^3\text{P}_2) + \epsilon d$ | $5s^2 5p^4 ({}^1\text{D}_2) + \epsilon d$ |
| $5s^2 5p^4 ({}^1\text{S}_0) nd {}^2\text{D}_{5/2}$ | $[02]_{5/2}$ | $5s^2 5p^4 ({}^3\text{P}_2) + \epsilon s/\epsilon d$ | $5s^2 5p^4 ({}^1\text{D}_2) + \epsilon s/\epsilon d$ |
| $5s^2 5p^4 ({}^1\text{S}_0) nd {}^2\text{D}_{3/2}$ | $[02]_{3/2}$ | $5s^2 5p^4 ({}^3\text{P}_2) + \epsilon s/\epsilon d$ | $5s^2 5p^4 ({}^1\text{D}_2) + \epsilon s/\epsilon d$ |

Table 5

Energy of resonances converging to the $\text{I}^+ ({}^1\text{S}_0)$ threshold at 14.109 eV, recorded in CIS spectra for the first, $\text{I}^+ ({}^3\text{P}_2) \leftarrow \text{I} ({}^2\text{P}_{3/2})$, band of iodine atoms at $\theta = 54^\circ 44'$. Also shown, are the effective and principal quantum numbers, n^* and n , the fitting parameters, q , Γ , ρ^2 and Γn^{*3} for each Rydberg state.

(i) ns [0] $\frac{1}{2}$ series

| E_n/eV | n^* | n | q | Γ/meV | Γn^{*3} |
|------------------------|--------------------|-----|---------------------|---------------------|--------------------|
| 13.258 ± 0.0008 | 4.00 ± 0.01 | 8 | -1.75 ± 0.35 | 8.5 ± 2.8 | 0.54 \pm 0.18 |
| 13.576 ± 0.002 | 5.50 ± 0.02 | 9 | -0.64 ± 0.55 | 8.6 ± 3.2 | 1.43 ± 0.53 |
| 13.736 ± 0.001 | 6.04 ± 0.03 | 10 | -1.78 ± 0.72 | 7.0 ± 2.6 | 1.55 ± 0.64 |
| not | seen | 11 | | | |
| 13.900 ± 0.001 | 8.06 ± 0.06 | 12 | -2.21 ± 1.41 | 4.5 ± 2.3 | 2.37 ± 1.21 |
| 13.951 ± 0.001 | 9.29 ± 0.10 | 13 | -0.89 ± 0.72 | 1.5 ± 3.1 | 1.20 ± 2.52 |
| | | | | | |

(i) nd $[2]_{5/2,3/2}$ series

| E_n/eV | n^* | n | q | Γ/meV | Γn^{*3} |
|-----------------------|---------------------|-----|--------------------|---------------------|--------------------|
| 13.056 ± 0.001 | 3.59 ± 0.01 | 6 | 2.30 ± 0.14 | 24.4 ± 1.8 | 1.13 ± 0.08 |
| 13.468 ± 0.001 | 4.61 ± 0.01 | 7 | 2.82 ± 0.18 | 12.2 ± 1.4 | 1.19 ± 0.14 |
| 13.681 ± 0.001 | 5.64 ± 0.02 | 8 | 2.69 ± 0.17 | 10.0 ± 1.0 | 1.79 ± 0.18 |
| 13.803 ± 0.001 | 6.66 ± 0.03 | 9 | 3.00 ± 0.42 | 6.9 ± 1.4 | 2.04 ± 0.40 |
| 13.878 ± 0.001 | 7.67 ± 0.05 | 10 | 2.09 ± 0.34 | 6.2 ± 1.8 | 2.82 ± 0.84 |
| 13.929 ± 0.001 | 8.70 ± 0.08 | 11 | 2.75 ± 0.82 | 6.3 ± 1.8 | 4.13 ± 1.21 |
| 13.966 ± 0.002 | 9.74 ± 0.12 | 12 | 2.84 ± 1.52 | 7.4 ± 1.5 | 6.83 ± 3.48 |
| 13.990 ± 0.002 | 10.70 ± 0.16 | 13 | 1.81 ± 1.01 | 6.5 ± 2.8 | 7.98 ± 3.48 |
| | | | | | |

Table 6

Ionisation energies and quantum defects obtained from the fit of series converging to the $\Gamma^+(^1S_0)$ threshold at 14.109 eV. Also shown, is the difference in meV from the value given in ref.(100) (14.109 eV).

| | | | E_{∞} (eV) | ΔE relative to the value in ref (100) (meV) | δ |
|-------------------------------------|--------------------------|----------------------|----------------------|--|-----------------|
| ns[0] _{1/2} series | $\theta = 0^{\circ}$ | 1 st band | 14.1114 ± 0.0027 | 2.4 | 3.79 ± 0.10 |
| | | 4 th band | 14.1121 ± 0.0039 | 3.1 | 3.77 ± 0.15 |
| | $\theta = 54^{\circ}44'$ | 1 st band | 14.1122 ± 0.0086 | 3.2 | 3.77 ± 0.36 |
| | | 4 th band | 14.1111 ± 0.0042 | 2.1 | 3.65 ± 0.15 |
| nd [2] _{5/2,3/2} series | $\theta = 0^{\circ}$ | 1 st band | 14.1116 ± 0.0021 | 2.6 | 2.35 ± 0.06 |
| | | 4 th band | 14.1116 ± 0.0013 | 2.6 | 2.24 ± 0.03 |
| | $\theta = 54^{\circ}44'$ | 1 st band | 14.1128 ± 0.0010 | 3.8 | 2.34 ± 0.30 |
| | | 4 th band | 14.1137 ± 0.0029 | 4.7 | 2.27 ± 0.07 |

Table 7

The asymmetry parameter, β , for different values of the angular momentum transfer quantum number, $j_t(102,103)^{(a)}$.

| j_t | l_{odd} | β | l_{even} | β |
|-------|------------------|---------|-------------------|---------|
| 0 | 1 | 2 | | |
| 1 | 1 | -1 | 0 | 0 |
| | | | 2 | 1 |
| 2 | 1 | 1/5 | 2 | -1 |
| | 3 | 4/5 | | |
| 3 | 3 | -1 | 2 | 2/7 |

| | | | | |
|---|---|-------|---|-------|
| | | | 4 | $5/7$ |
| | | | | |
| 4 | 3 | $3/9$ | 4 | -1 |
| | 5 | $6/9$ | | |
| | | | | |

(a) The angular momentum transfer is defined as the angular momentum transferred between that atom, and the ion and photoelectron (see text).

Figure Captions

Figure 1

A schematic potential energy diagram at a photon energy which gives resonant ionization

Figure 2

HeI photoelectron spectrum recorded for discharged oxygen. In this figure, the numbers used to label bands associated with the ionizations are as follows:-

1. $O_2^+(X^2\Pi_g) \leftarrow O_2(a^1\Delta_g)$; 2. $O_2^+(X^2\Pi_g) \leftarrow O_2(X^3\Sigma_g^-)$;
3. $O^+(^4S) \leftarrow O(^3P)$; 4. $O_2^+(a^4\Pi_u) \leftarrow O_2(X^3\Sigma_g^-)$; $O_2^+(A^2\Pi_u) \leftarrow O_2(X^3\Sigma_g^-)$;
5. $O^+(^2D) \leftarrow O(^3P)$; 6. $O_2^+(A^2\Pi_u) \leftarrow O_2(X^3\Sigma_g^-)$; $O_2^+(C^2\Phi_u) \leftarrow O_2(a^1\Delta_g)$;
7. $O_2^+(b^4\Sigma_g^-) \leftarrow O_2(X^3\Sigma_g^-)$; 8. $O_2^+(D^2\Delta_g) \leftarrow O_2(a^1\Delta_g)$;
9. $O_2^+(B^2\Sigma_g^-) \leftarrow O_2(X^3\Sigma_g^-)$;

(Reproduced from ref.(29) with permission of AIP Publishing).

Figure 3

CIS spectra recorded for $O_2^+(X^2\Pi_g)v^+ \leftarrow O_2(a^1\Delta_g)v'' = 0$ over the photon energy region 14.0–15.0 eV, for $v^+ = 0, 1, 2, 3$. The black circles indicate the computed CIS relative intensities obtained from Franck–Condon calculations (see the text). (Reproduced from ref.(29) with permission of AIP Publishing).

Figure 4

Photoelectron spectra recorded at $h\nu = 14.37$ eV (i.e. at the position of band B in Fig. 3) for discharged and undischarged oxygen, in the ionization energy region 11.0–14.4 eV. The black circles in the lower part of this figure represent computed relative vibrational intensities obtained by summing the direct and autoionization computed envelopes (see the text). (Reproduced from ref.(29) with permission of AIP Publishing).

Figure 5

HeI photoelectron spectra recorded for a flowing SO_2/Ar mixture. (a) recorded with the microwave discharge off, and (b) recorded with the microwave discharge on. (Reproduced from ref.(27) with permission of AIP Publishing).

Figure 6

CIS spectra recorded for $\text{SO}^+ \text{b}^4\Sigma^-$, $v^+ \leftarrow \text{SO X}^3\Sigma$, $v''=0$, for $v^+ = 0$ and $v^+ = 1$ in the photon energy range 15.1–16.4 eV. (Reproduced from ref.(27) with permission of AIP Publishing).

Figure 7

Photoelectron spectra of the fourth band of SO recorded at photon energies of (a) 21.218, (b) 15.535, (c) 15.855, and (d) 15.970 eV. (Reproduced from ref.(27) with permission of AIP Publishing).

Figure 8

TPE (upper) and PE (lower, photon energy 21.0 eV) spectra recorded for a flowing CF_2 and Ar mixture in the 11.3–13.2 eV ionization energy region. (Reproduced from ref.(39) with permission from Wiley-VCH Verlag GmbH & Co. KGaA).

Figure 9

Expanded TPE spectrum of CF_2 in the 11.4–12.2 eV photon energy region (upper). Simulated $\text{CF}_2^+ (\text{X}^2\text{A}_1) \leftarrow \text{CF}_2(\text{X}^1\text{A}_1)$ photoelectron spectrum for 0 K Boltzmann vibrational temperature (lower). (Reproduced from ref.(39) with permission from Wiley-VCH Verlag GmbH & Co. KGaA).

Figure 10

Expanded TPE spectrum of CF_2 in the 11.4–12.2 eV photon energy region (upper). Simulated $\text{CF}_2^+ (\text{X}^2\text{A}_1) \leftarrow \text{CF}_2(\text{X}^1\text{A}_1)$ photoelectron spectrum for 600 K Boltzmann vibrational temperature (lower). (Reproduced from ref.(39) with permission from Wiley-VCH Verlag GmbH & Co. KGaA).

Figure 11

A simulated spectrum showing assignment of the main structure in the low energy region (11.3–12.2 eV) in the first photoelectron band of CF_2 . The doublet structure observed in some of the bands arises because $2v_2^+$ is approximately equal to v_1^+ . The main structure shown corresponds to $(v_1^+, v_2^+, 0) \leftarrow (0, 0, 0)$ combination bands with v_1^+ and $v_2^+ = 0, 1, 2$ and 3. (Reproduced from ref.(39) with permission from Wiley-VCH Verlag GmbH & Co. KGaA).

Figure 12

PE spectrum recorded for the $F + CH_2I_2$ reaction at $h\nu = 21.22$ eV at $\theta = 54^\circ 44'$ and 3 cm mixing distance above the photon beam showing a “low” I to IF ratio (see text). (Reproduced from ref.(23) with permission of ACS Publishing).

Figure 13

TPE spectrum recorded for the $F + CH_2I_2$ reaction in the 10.3 - 12.3 eV photon energy region at a mixing distance of 3 cm above the photon beam. (Reproduced from ref.(23) with permission of ACS Publishing).

Figure 14

CIS spectra of the first PE band of iodine atoms ($I^+(^3P_2) \leftarrow I(^2P_{3/2})$) recorded at an angles of (a) $\theta = 0^\circ$ and (b) $\theta = 54^\circ 44'$ in the photon energy region 12.9 to 14.1 eV, showing autoionizing resonances converging to the $I^+(^1S_0)$ threshold at 14.109 eV. (Reproduced from ref.(40) with permission of AIP Publishing)

Figure 15

Beta plots recorded over the photon energy region 12.9 to 14.1 eV. Spectrum (a) was recorded for the $I^+(^3P_2) \leftarrow I(^2P_{3/2})$ band of iodine atoms whereas spectrum (b) was recorded for the $I^+(^1D_2) \leftarrow I(^2P_{3/2})$ band of iodine atoms. The resonance positions in the CIS spectra have been marked on for reference. (Reproduced from ref.(40) with permission of AIP Publishing)

References

1. Special Issue on Reactive Intermediates Chemical Reviews 2013, **113**, 6903-7342
Edited by R.A.Moss
2. J.M.Dyke, M.V.Ghosh, M. Goubet, E.P.F.Lee, G.Levita, K.Miqueu and D.E.Shallcross A study of the atmospherically relevant reaction between molecular chlorine and dimethyl sulphide (DMS): Establishing the reaction intermediate and measurement of absolute photoionisation cross-sections Chemical Physics 2006, **324**, 85-95
3. J.M.Dyke, M.V.Ghosh, D.J.Kinnison, G.Levita, A.Morris and D.E. Shallcross A kinetics and mechanistic study of the atmospherically relevant reaction between molecular chlorine and dimethyl sulphide (DMS) PCCP 2005, **7**, 866-873
4. J.M.Dyke, S.D.Gamblin, N.Hooper, E.P.F.Lee, A.Morris, D.K.W.Mok, and F.T.Chau A Study of BrO and BrO₂ with vacuum ultraviolet photoelectron spectroscopy J.Chem Phys 2000, **112**, 6262-6274

5. J.H.D.Eland Photoelectron Spectroscopy, Butterworths London 1974
6. J.Berkowitz Photoionization mass spectrometric studies of free radicals
Acc Chem Res 1989, **22**, 413-420
7. J.M.Dyke, N.Jonathan and A.Morris Recent Progress in the Study of Transient Species with Vacuum Ultraviolet Photoelectron Spectroscopy,
International Review of Physical Chemistry 1982, **2**, 3-42
8. J.M.Dyke, N.Jonathan and A.Morris Vacuum Ultraviolet Photoelectron Spectroscopy of Transient Species Electron Spectroscopy 1979, **3**, 189-224
Edited by C.R.Brundle and A.D.Baker, Academic Press London
9. M.C.R.Cockett, J.M.Dyke and H.Zamanpour Photoelectron Spectroscopy of Short-Lived Molecules in Vacuum Ultraviolet Photoionization and Photodissociation of Molecules and Clusters Edited by C.Y.Ng, World Scientific Co., New Jersey, 1991, 43-99
10. J.M.Dyke Properties of gas-phase ions J.C.S Faraday II 1987, **83**, 67-87
11. P.Chen Photoelectron Spectroscopy of Reactive Intermediates in Unimolecular and Bimolecular Reaction Dynamics, 1984, 372-425
Edited by C.Y.Ng, T. Baer and I.Powis, John Wiley and Sons
12. S.Willitsch, F.Innocenti, J.M.Dyke and F. Merkt High-resolution pulsed-field-ionization zero-kinetic-energy photoelectron spectroscopic study of the two lowest electronic states of the ozone cation O_3^+ J.Chem Phys 2005, **122**, 024311
13. J.M.Dyke, L. Golob, N.Jonathan, A.Morris and M. Okuda Vacuum Ultraviolet Photoelectron Spectroscopy of Transient Species: Part 4 Difluoromethylene and Ozone J.C.S.Faraday Trans II, 1974, **70**, 1828-1836
14. S. Katsumata, H.Shiromaru and T. Kimura T. Photoelectron Angular Distributions and Assignment of the Photoelectron Spectrum of Ozone
Bull Chem Soc Jap. 1984, **57**, 1784-1788
15. C.R.Brundle C.R. He(I) and He(II) photoelectron spectrum of ozone
Chem Phys Letts 1974, **26**, 25-28
16. D.C.Frost, S.T.Lee and C.A.McDowell
High resolution photoelectron spectroscopy of ozone Chem Phys Letts 1974, **24**, 149-152
17. M.J.Weiss, J. Berkowitz and E.H.Appelman Photoionization of ozone: Formation of O_4^+ and O_5^+ J.Chem Phys 1977, **66**, 2049-2053
18. J.T.Moseley, J.B.Ozenne and P.C.Crosby Photofragment spectroscopy of O_3^+ J.Chem Phys 1981, **74**, 337-992
19. M.Probst, K.Hermansson, J.Urban, P.Mach, D.Mugg, G.Denifl, T.Fiegele, N.J.Mason, A.Stamotovoic and T.D.Mark Ionization energy studies of ozone and OCIO monomers and dimers J.Chem Phys 2002, **116**, 984-992

20. W.A. Chupka Effect of Unimolecular Decay Kinetics on the Interpretation of Appearance Potentials J.Chem Physics 1959, **30**, 191-211
21. B.Sztaray, A.Bodi and T.Baer Modeling unimolecular reactions in photoelectron photoion coincidence experiments J.Mass Spectrom 2010, **45**, 1233-1245
22. W.C.Price NeI and HeI photoelectron spectra of molecular oxygen
Molecular Spectroscopy edited by P.Hepple Elsevier, New York, 1968 , vol. **4**, 221-226
23. A Study of the Reactive Intermediate IF and I Atoms with Photoelectron Spectroscopy F.Innocenti, M.Eypper, S. Beccaceci, A. Morris, S. Stranges, J. B. West, G. C. King, and J. M. Dyke J.Phys.Chem A 2008, **112**, 6939 – 6949
24. Photoelectron spectroscopy of short-lived molecules using synchrotron radiation. J.B. West, J.M. Dyke, A. Morris, T.G. Wright and S.D. Gamblin
J. Phys. B, 1999, **32**, 2763-2782
25. A photoelectron spectrometer for studying reactive intermediates using synchrotron radiation
J.M. Dyke, S.D. Gamblin, A. Morris, T.G. Wright, A.E. Wright and J.B. West
J. Electron Spec Rel Phen 1998, **97**, 5-14
26. Studies of Reactive Intermediates with Synchrotron Radiation: SO($X^3\Sigma^-$)
J.M. Dyke, D. Haggerston, A. Morris, S. Stranges, J.B. West and A.E. Wright.
J.Elect. Spec. Rel. Phen. 1995, **76**, 165-170
27. A Study of the SO Molecule with Photoelectron Spectroscopy using Synchrotron Radiation J.M. Dyke, D. Haggerston, A. Morris, S. Stranges, J.B. West, T.G. Wright and A.E. Wright J. Chem Phys 1997, **106**, 821-830
28. A Study of the CS molecule with photoelectron spectroscopy using synchrotron radiation
J.M. Dyke, S.D. Gamblin, D. Haggerston, A. Morris, S. Stranges, J.B. West, T.G. Wright and A.E. Wright J. Chem Phys 1998, **108**, 6258-6265
29. A study of O₂($a^1\Delta_g$) with photoelectron spectroscopy using synchrotron radiation J.D. Barr, A. De Fanis, J.M. Dyke, S.D. Gamblin, A. Morris, S. Stranges, J.B. West, T.G. Wright and A.E. Wright J. Chem Phys 1998, **109**, 2737-2747
30. Study of the OH and OD radicals with photoelectron spectroscopy using synchrotron radiation
J.D. Barr, A. De Fanis, J.M. Dyke, S.D. Gamblin, N. Hooper, A. Morris, S. Stranges, J.B. West and T.G. Wright
J. Chem Phys 1999, **110**, 345-354
31. Angle Resolved Photoelectron Spectroscopy of O₂($a^1\Delta_g$) with Synchrotron Radiation
L. Beeching, A. De Fanis, J.M. Dyke, S.D. Gamblin, N. Hooper, A. Morris and J.B. West.
J. Chem. Phys., 2000, **112**, 1707-1712

32. Photoelectron spectroscopy of reactive intermediates using synchrotron radiation J.D.Barr, L. Beeching, A.De Fanis, J.M. Dyke, S.D. Gamblin, N. Hooper, A.Morris, S.Stranges, J.B.West, A.E.Wright, and T.G.Wright J.Elec.Spec. Rel. Phen. 2000, **108** , 47-61
- 33.Photoelectron Spectroscopy of atomic oxygen using the Elettra Synchrotron source L.J.Beeching, A.A.Dias, J.M.Dyke, A.Morris, S.Stranges, J.B.West, N.Zema and L.Zuin Molecular Physics 2003, **101**, 575-582
- 34.An initial investigation of S and SH with angle resolved photoelectron spectroscopy using synchrotron radiation L.Zuin, F.Innocenti, M.L.Costa, A.A.Dias, A.Morris, A.C.S. Paiva, S.Stranges, J.B.West and J.M.Dyke Chemical Physics 2004, **298**, 213-222
35. Photoionization Studies of the Atmospherically Important Species N and OH at the Elettra Synchrotron Radiation Source F.Innocenti, L.Zuin, M.L.Costa, A.A.Dias, A.Morris, A.C.S.Paiva, S.Stranges, J.B.West and J.M.Dyke J.Elec. Spec. Rel. Phen 2005, **142**, 241-252
- 36.A study of the NO Radical with PE and CIS spectroscopy:
Investigation of Rydberg states above the first ionization threshold F. Innocenti , A. A.Dias , M.Goubet , R.I.Oleriu, M. L.Costa, A. Morris, S. Stranges, L. Zuin and J. M.Dyke Mol. Phys 2007, **105**, 771-796
37. A study of the CF Radical with PE and CIS spectroscopy: Investigation of Rydberg states above the first ionization threshold F. Innocenti , A.A.Dias , M.Goubet , R.I.Oleriu, M. L.Costa, A. Morris, S. Stranges, L. Zuin and J.M.Dyke Mol. Phys 2007, **105**, 755-769
38. Measurement of the partial photoionization cross-sections and asymmetry parameters of S atoms in the photon energy range 10.0-30.0 eV using constant-ionic-state (CIS) spectroscopy F.Innocenti, L.Zuin, M.L.Costa, A.A.Dias, A.Morris, S.Stranges, and J.M.Dyke J.Chem Phys 2007, **126**, 154310-154313
39. Difluorocarbene studied with Threshold Photoelectron Spectroscopy (TPES): Measurement of the first Adiabatic Ionization Energy (AIE) of CF₂ F. Innocenti, M.Eyyper, E. P.F.Lee, S. Stranges, D. K.W.Mok, F.T. Chau, G. C. King, and J.M. Dyke Chem.Eur. J. 2008, **14**, 11452-11460
40. Photoionization of iodine atoms: Rydberg series which converge to the I⁺(¹S₀) ← I(²P_{3/2}) threshold M.A.Eyyper, F.Innocenti, A.Morris, S.Stranges, G.C.King and J.M.Dyke J.Chem Phys 2010, **132**, 244304
41. Photoionization of iodine atoms: Angular distributions and relative partial photoionization cross-sections in the energy region 11.0-23.0 eV M.Eyyper, F.Innocenti, A.Morris, S.Stranges, J.B.West, G.C.King and J.M.Dyke J.Chem. Phys 2010, **133**, 084302

42. Threshold photoelectron spectroscopy (TPES) of vibrationally excited nitrogen F.Innocenti, M.Eypper, S.Stranges, J.B. West, G.C. King and J.M.Dyke J.Physics B 2013, **46**, 045002-045009
43. A Study of H₂O₂ with Threshold Photoelectron Spectroscopy (TPES) and Electronic Structure Calculations: Re-determination of the first Adiabatic Ionization Energy (AIE)
L.Schio, M.Alagia, A. A. Dias, S.Falcinelli, V.Zhaunerchyk, E.P.F.Lee, D.K.W.Mok, J.M. Dyke and S.Stranges J.Phys Chem A 2016, **27**, 5220-5229
- 44.P.Oswald, P.Hemberger, T.Bierkandt, E.Akyildiz, M.Kohler, A.Bodi, T.Gerber and T.Kasper *In situ* flame chemistry tracing by imaging photoelectron photoion coincidence spectroscopy Rev Sci Instrument 2014, **85**, 025101
45. Synchrotron-based double imaging photoelectron/photoion coincidence spectroscopy of radicals produced in a flow-tube: OH and OD
G.A.Garcia, X.Tang, J.F.Gil, L.Nahon, M.Ward, S.Batut, C.Fittschen, C.A.Taatjes and D.L.Osborn J.Chem Phys 2015, **142**, 164201
46. Synchrotron based valence shell photoionization of CH radical
B.Gans, F.Holzmeier, J.Kruger, C.Falvo, A.Roder, A.Lopes, G.A.Garcia, C.Fittschen, J.C.Loison, and C.Alcaraz J.Chem Phys 2016, **144**, 204307
47. Unveiling the Ionization Energy of the CN radical
B.Gans, S.Boye-Peronne, G.A.Garcia, A.Roder, D.Schleier, P.Halvick, sand J.C.Loison J.Phys Chem Letts 2017, **8**, 4038-4042
48. Threshold photoelectron spectroscopy of the imidogen radical
G.A.Garcia, B.Gans, X.Tang, M.Ward, S.Batut, L.Nahon, C.Fittschen and J.C. Loison J.Elec Spec Rel Phen 2015, **203**, 25-30
- 49.Probing Phosphorus Nitride (PN) and other elusive species formed upon pyrolysis of dimethyl phosphoramidate
S.Liang, P.Hemberger, J.Levalois-Grutzmacher, H.Grutzmacher and S.Gaan Chem Eur 2017, **23**, 5595-5601
50. Elucidating the thermal decomposition of dimethyl methyl phosphonate by vacuum ultraviolet (VUV) photoionization: pathways to the PO radical, a key species in flame-retardant mechanisms
S.Liang, P.Hemberger, N.M. Neisius, A.Bodi, H.Grutzmacher, J.Levalois-Grutzmacher and S.Gaan Chem Eur J 2015, **21**, 1073-1080
51. Communication: On the first ionization threshold of the C₂H radical
B.Gans, G.A.Garcia, F.Holzmeier, J.Kruger, A.Roder, A.Lopes, C.Fittschen, J.C.Loison, amd C.Alcaraz J.Chem Phys 2017, **146**, 011101
52. Valence shell threshold photoelectron spectroscopy of the CH_xCN (x=0-2) and CNC radicals G.A.Garcia, J.Kruger, B.Gans, C.Falvio, L.H.Coudert and J.C.Loison J.Chem Phys 2017, **147**, 013908

53. Valence shell threshold photoelectron spectroscopy of C_3H_x ($x=0-3$).
G.A.Garcia, B.Gans, J.Kruger, F.Holzmeier, A.Roder, A.Lopes, C.Fittschen, C.Alcaraz, and J.C.Loison PCCP 2018, **20**, 8707-8718

54. Assignment of high-lying bending mode levels in the threshold photoelectron spectrum of NH_2 : a comparison between pyrolysis and fluorine-atom abstraction radical sources
F.Holzmeier, M.Lang, I.Fischer, P.Hemberger, G.A.Garcia, X.Tang and J.C.Loison PCCP 2016, **17**, 19507-19514

55. Threshold photoelectron spectroscopy of the methyl radical isotopomers, CH_3 , CH_2D , CHD_2 and CD_3 : Synergy between VUV synchrotron radiation experiments and explicitly coupled cluster calculations
B.K.C.de Miranda, C.Alcaraz, M.Elhanine, B.Noller, P.Hemberger, I.Fischer, G.A.Garcia, H.Soldi-Lose, B.Gans, L.A.V.Mendes, S.Boye-Peronne, S.Douin, J.Zabka and P.Botschwina J.Phys Chem A 2010, **114**, 4818-4830

56. Comprehensive vacuum ultraviolet photoionization study of the CF_3 trifluoromethyl radical using synchrotron radiation
H.Dossman, G.A.Garcia, L.Nahon, B.K.C.de Miranda, and C.Alcaraz J.Chem Phys 2012, **136**, 204304

57. Photoionization of two substituted methyl radicals: cyanomethyl and bromomethyl
M.Steinbauer, P.Hemberger, I.Fischer, M.Johnson and A.Bodi Chem Phys Letts 2010, **500**, 232-236

58. CRF-PEPICO: Double velocity map imaging photoelectron photoion coincidence spectroscopy for reaction kinetics studies
B.Sztaray, K.Voronova, K.G.Torma, K.J.Covert, A.Bodi, P.Hemberger, T.Gerber, and D.L.Osborn J.Chem, Phys 2017, **147**, 013944

59. D.Schleier, A.Humeniuk, E.Reusch, F.Holzmeier, D.Nunez-Reyes, C.Alcaraz, G.A.Garcia, J.C.Loison, I.Fischer and R.Mitric Diborene: Generation and Photoelectron Spectroscopy of an Inorganic Radical J.Physical Chemistry Letters 2018, **9**, 5921-5925

60. B.Gans, G.A.Garcia, S.Boye-Peronne, S.T.Pratt, J.C. Guillemin, A.Aquado, O.Roncero and J.C. Loison Origin band of the first photoionizing transition of hydrogen isocyanide PCCP 2019, **21**, 2337-2344

61. L.H.Codert, B.Gans, F.Holzmeier, J.C.Loison, G.A.Garcia, C.Alcaraz, A.Lopez, and A.Roder Experimental and theoretical threshold photoelectron spectra of methylene J.Chem Phys 2018, **149**, 224304 (10 pages).

62. J.M.Dyke, L.Golob, N.Jonathan, A.Morris and M.Okuda
Vacuum ultraviolet photoelectron spectroscopy of transient species Part 3 The $SO(^3\Sigma^-)$

- radical J.C.S.Faraday Trans II 1974, **70**, 1818-1827
63. N.Jonathan, A.Morris, M.Okuda, K.J.Ross and D.J.Smith Photoelectron spectroscopy of transient species-the CS molecule Faraday Discussions 1972, **54**, 48-55
 64. N.Jonathan, A.Morris, M.Okuda, K.J.Ross and D.J.Smith Vacuum Ultraviolet Photoelectron Spectroscopy of Transient Species 2 Use of phase sensitive detection for investigating electronic states of O_2^+
J.C.S.Faraday II 1974, **70**, 1810-1817
 65. S.Katsumata and D.R.Lloyd
Photoelectron spectrum of OH and OD Chem Phys Letts 1977, **45**, 519-522
 66. H.van Lonkhuyzen and C.A.de Lange
UV photoelectron spectroscopy of OH and OD radicals
Molecular Physics 1984, **51**, 551-568
 67. N.Jonathan, A.Morris, D.J.Smith and K.J.Ross Photoelectron spectra of ground state atomic hydrogen, nitrogen and oxygen Chem Phys Letts 1970, **7**, 497-499
 68. The HeI photoelectron spectrum of the $SH(X^2\pi)$ radical.
J.M. Dyke, N. Jonathan, N.K. Fayad and A. Morris.
Molecular Physics, 1979, **38**, 729-738; 1981, **44**, 265-269.
 69. O.Edqvist, E.Lindolm, L.E.Selin, H.Sjogren, and L.Asbrink Rydberg series in small molecules 7. Rydberg series and photoelectron spectroscopy of NO
Arkiv for Fysik 1970, **40**, 439-448
 70. J.M. Dyke, A.E. Lewis and A. Morris.
A photoelectron spectroscopic study of the ground state of CF^+ via the ionization process $CF^+(X^1\Sigma^+) \leftarrow CF(X^2\Pi)$. J. Chem. Phys. 1984, **80**, 1382--1386
 - 71.E.A. Colbourn, J.M. Dyke, N.K. Fayad and A. Morris.
The photoelectron spectra of IF and BrF.
J. Electron Spectroscopy Rel. Phen., 1978, **14**, 443-452
 72. J.Berkowitz and G.L.Goodman Partial photoionisation cross sections of atomic iodine – irreducible tensor analysis of intensities J.Chem Phys 1979, **71**, 1754-1760
 73. J.M.Dyke,L.Golob, N.Jonathan and A.Morris
Photoelectron spectra of transient species: vibrationally excited nitrogen and hydrogen
J.C.S. Faraday Trans II 1976, **72**, 597-603
 74. F.S.Ashmore, and A.R. Burgess Study of some medium size alcohols and hydroperoxides by photoelectron spectroscopy J.C.S. Faraday II 1977, **73**, 1247-1261.
 75. J.M.Dyke, S.J.Dunlavey,N.Jonathan and A.Morris
The HeI photoelectron spectrum of the NH_2 radical

Molecular Physics 1980, **39**, 1121-1135

76. D.K. Bulgin, J.M. Dyke and A. Morris

The HeI photoelectron spectrum of the PN ($X^1\Sigma^+$) molecule
J.C.S. Faraday II 1977, **73**, 983-990

77. J.M. Dyke, A.M.A. Ridha, and A. Morris

Characterization of the ground state of PO^+
J.C.S. Faraday 1982, **78**, 2077-2082

78. J.M. Dyke, E.P.F. Lee, A. Morris and N. Jonathan

The photoelectron spectrum of the methyl radical
J.C.S. Faraday II 1976, **72**, 1385-1396

79. L. Andrews, J.M. Dyke, N. Jonathan, N. Keddar and A. Morris

The first bands in the photoelectron spectra of CH_2Br , CD_2Br , $CHBr_2$ and CH_2I
free radicals J. Physical Chemistry 1984, **88**, 1950-1954

80. D.H. Katayama, R.E. Huffman and Y. Tanaka $O_2(a^1\Delta_g)$ absorption bands in the vacuum
ultraviolet J. Chem. Phys 1975, **62**, 2939-2948

81. R.E. Huffman, J.C. Larrabee, and Y. Tanaka New absorption spectra of atomic and
molecular oxygen in the vacuum ultraviolet I. Rydberg series from OI ground state and new
excited O_2 bands J. Chem Phys 1967, **46**, 2213-2233

82. D.H. Katayama, S. Ogawa, M. Ogawa and Y. Tanaka

The vacuum uv absorption spectrum of O_2 from its metastable states $b^1\Sigma_g^+$ and $a^1\Delta_g$
J. Chem Phys 1977, **67**, 2132-2142

83. D. Dill Resonances in Photoelectron Angular Distributions

Phys Rev A 1973, **7**, 1976-1987

84. P.M. Guyon, R. Spohr, W.A. Chupka and J. Berkowitz, Threshold photoelectron spectra
of HF, DF and F_2 J. Chem. Phys. 1976, **65**, 1650-1658

85. T. Baer and P.M. Guyon, Autoionization and isotope effect in the threshold photoelectron
spectrum of $^{12}CO_2$ J. Chem. Phys. 1986, **85**, 4765-4778

86. J.P.Booth Optical and electrical diagnostics of fluorocarbon plasma etching processes
Plasma Sources Sci Technol 1999, **8**, 249-257
87. T.J.Buckley, R.D.Johnson, R.E.Huie, Z.Zhang, S.C.Kuo and R.B.Klemm Ionization energies, appearance energies and thermochemistry of CF_2O and FCO
J.Phys Chem 1995, **99**, 4879-4885
88. V.Tarnovsky and K.Becker Absolute partial cross-sections for the parent ionization of the CF_x ($x=1-3$) free radicals J.Chem Phys 1993, **99**, 7868-7874
89. S.J. Davis and A.M. Woodward Excitation of IF ($\text{B}^3\Pi, 0^+$) by metastable O_2 1. Studies involving $\text{IF}(X,v)$ J.Phys Chem. 1991, **95**, 4610-4618
90. K.Y. Kane and J.G. Eden, Enhanced performance of the iodine monofluoride (491nm) laser
IEEE J. Quantum Electronics 1990, **26**, 1620-1623
- 91.V.F. Gavrikov, A.N. Dvoryankin, A.A. Stepanov, A.K. Shmelev and V.A. Shcheglov,
Visible and near-infrared chemical lasers J. Russian Laser Research 1994, **15**, 177-212
92. A.J. Cormack, A.J. Yench, R.J. Donovan, K.P. Lawley, A. Hopkirk and G.C. King,
High resolution photoelectron spectroscopy of molecular fluorine
Chemical Physics 1996, **213**, 439-448
93. A.J. Yench, A. Hopkirk, A. Hiraya, R.J. Donovan, J.G. Goode, R.R.J. Maier, G.C. King
and A. Kvaran, Threshold photoelectron spectroscopy of Cl_2 and Br_2
J. Phys. Chem. 1995, **99**, 7231-7241
94. A.J. Yench, M. Cristina Lopes and G.C. King, Threshold photoelectron spectroscopy of
iodine monochloride Chem. Phys. Letts. 2000, **325**, 559-567
95. A.J. Yench, A.E.R. Malins and G.C. King, Threshold photoelectron spectroscopy of
iodine monobromide Chem. Phys. Letts. 2003, **370**, 756-764

96. D.M.de Leeuw, R. Mooyman and C.A. de Lange He(I) photoelectron spectrum of halogen atoms Chem Phys Letts 1978, **54**, 231-234
97. National Institute of Standards and Technology, Physics Laboratory Physical Reference Data. <http://physics.nist.gov/PhysRefData>
98. R.E. Huffman, J.C. Larrabee and Y. Tanaka Comment on absorption series and ionization potentials of atomic chlorine and iodine J.Chem. Phys. 1968, **48**, 3835
99. R.E. Huffman, J.C. Larrabee and Y. Tanaka New absorption series and ionization potentials of atomic fluorine, chlorine, bromine and iodine J.Chem Phys 47, 1967, 856-857;
Comment on absorption series and ionization potentials of atomic chlorine and iodine J.Chem Phys 1968, **48**, 3835 (1 page)
100. J. Berkowitz, C. Batson and G. Goodman Photoionization of atomic iodine and tellurium Phys Rev A 1981, **24**, 149-160
101. J. Cooper and R.N. Zare Photoelectron Angular Distributions Lect Theor Phys 11C, 1969, 317-337 in Atomic Collision Processes Editors S. Geltman, K.T. Mahanthappa, W.E. Brittin Publ. Gordon and Breach, Science Publ., New York, 1969
102. D. Dill and U. Fano Parity unfavoredness and distribution of photofragments Phys Rev Lett 1972, **29**, 1203-1205
103. E.S. Chang Proceedings of the Daresbury One Day Meeting in Photoionisation of Atoms and Molecules, edited by B.D. Buckley (Daresbury Labs, Daresbury UK, 1978) 23-33
104. J.Z. Wu, S.B. Whitfield, C.D. Caldwell, M.O. Krause, P. van der Meulen and A. Fahlman High resolution photoelectron spectrometry of selected ns' and nd' autoionization resonances in Ar, Kr and Xe Phys Rev A 1990, **42**, 1350-1357
105. J.A.R. Samson and J.L. Gardner Resonances in angular distribution of xenon photoelectrons Phys Rev Lett 1973, **31**, 1327-1357

106. W.R.Johnson, K.T.Cheng, K.N.Huang and M.Ledourneuf
Analysis of Beutler-Fano autoionising resonances in the rare gas atoms using the relativistic multichannel quantum defect theory *Phys Rev A* 1980, **22**, 989-997

107. F.Robicheaux and C.H.Greene Regularities in calculated photoionization cross sections for the halogens *Phys Rev A* 1992, **46**, 3821-3833

108. F.Combet Faknoux and M.Ben Amar
Inner and outer shell ionization for atomic iodine: calculation of cross-sections and angular distribution parameters *J.Electron Spectrosc Relat.Phenom.* 1986, **41**, 67-87

109. S.T.Manson, A.Msezane, F.Starace and S. Shahabi Photoionization of chalcogen and halogen atoms: cross-sections and angular distributions *Phys Rev A* 1979, **20**, 1005-1018

110. J.H.D.Eland Photoelectron-Photoion Coincidence Spectroscopy I. Basic Principles and Theory *International J.Mass Spectrometry and Ion Physics* 1972, **8**, 143-151

111. T.Baer and R.P.Tuckett Advances in threshold photoelectron spectroscopy (TPES) and threshold photoelectron-photoion coincidence (TPEPICO) *PCCP* 2017, **19**, 9698-9723

112. T.Baer and Y.Li Threshold photoelectron spectroscopy with velocity focusing: an ideal match for coincidence studies *Int J Mass Spectrom* 2002, **219**, 381-389

113. B.Sztaray and T.Baer Suppression of hot electrons in threshold photoelectron photoion coincidence spectroscopy using velocity focusing optics *Rev Sci Instrum* 2003, **74**, 3763-3767

114. G.A.Garcia, H.Soldi-Lose and L.Nahon A versatile electron-ion coincidence spectrometer for photoelectron momentum imaging and threshold spectroscopy on mass selected ions using synchrotron radiation *Rev Sci Instrum* 2009, **80**, 023102 (10 pages)

115. G.Garcia, L.Nahon and I. Powis Two dimensional charged particle image inversion using a polar basis function expansion *Rev Sci Istrum* 2004, **75**, 4989-4996

116. J.C.Pouilly, J.P.Schermann, N.Nieuwjaer, F.Lecomte, G.Gregoire, C.Desfrancois, G.A.Garcia, L.Nahon, D.Nandi, L.Poisson and M.Hochlaf Photoionization of 2-pyridone and 2-hydroxypyridine PCCP 2010, **12**, 3566-3572
117. A.M.Chartrand, E.F.McCormack, U.Jacovella, D.M.P.Holland, B.Gans, X.Tang, G.A.Garcia, L.Nahon and S.T.Pratt Photoelectron angular distributions from rotationally resolved autoionizing states of N₂ J.Chem Phys 2017, **147**, 224303 (9 pages)
118. D.M.P.Holland, E.A.Seddon, S.Daly, C.Alcaraz, C.Romanzin, L.Nahon and G.A.Garcia. The effect of autoionization on the N₂⁺ X²Σ_g⁺ state vibrationally resolved photoelectron anisotropy parameters and branching ratios J.Physics B 2013, **46**, 095102 (10 pages)
119. X.Tang, X.Zhou, M.Niu, S.Liu, J.Sun, X.Shan, F.Liu and L.Sheng A threshold photoelectron-photoion coincidence spectrometer with double velocity imaging using synchrotron radiation Rev Sci Instrum 2009, **80**, 113101 (10 pages)
120. A.Bodi, M.Johnson, T.Gerber, Z.Gengelicki, B.Sztaray, and T.Baer Imaging photoelectron photoion coincidence spectroscopy with velocity focusing electron optics Rev Sci Instrum 2009, **80**, 034101 (7 pages)
121. A.Bodi, P.Hemberger, T.Gerber and B.Szrtaray A new double imaging velocity focusing coincidence experiment: i²PEPICO Rev Sci Instrum 2012, **83**, 083105 (8 pages)
122. G.A.Garcia, B.K.Cunha de Miranda, M.Tia, S.Day and L.Nahon DELICIOUS III: A multipurpose double imaging particle coincidence spectrometer for gas phase vacuum ultraviolet photodynamics studies Rev Sci Instrum 2013, **84**, 053112 (11 pages).
123. T.Baer, J.Booze and K.M.Weitzel in Vacuum Ultraviolet Photoionization and Photodissociation of Molecules and Clusters, edited by C.Y.Ng, World Scientific Singapore, 1991, 259-296
124. G.K.Jarvis, K.M.Weitzel, M.Malow, T.Baer, Y.Song, and C.Y.Ng High resolution pulse field ionization photoelectron-photoion coincidence spectroscopy using synchrotron radiation Rev Sci Instrum 1999, **70**, 3892-3906

125. C.Alcaraz, C.Nicolas, R.Thissen, J.Zabka and O.Dutuit
 $^{15}\text{N}^+ + \text{CD}_4$ and $\text{O}^+ + ^{13}\text{CO}_2$ state-selected ion molecule reactions relevant to the chemistry of planetary atmospheres. *J.Phys Chem A* 2004, **108**, 9998-10009
- 126.A.Bodi, B.Sztaray, T.Baer, M.Johnson and T.Gerber Data acquisition schemes for continuous two-particle time-of-flight coincidence experiments
Rev Sci Instruments 2007, **78**, 084102 (7 pages)
127. D.L.Osborn, C.C.Hayden, P.Hemberger, A.Bodi, K.Voronova, and B.Sztaray
 Breaking through the false coincidence barrier in electron-ion coincidence experiments
J.Chem Phys 2016, **145**, 164202 (8 pages)
- 128.F.Qi Combustion chemistry probed by synchrotron VUV photoionisation mass spectrometry *Proceedings of the Combustion Inst.* 2013, **34**, 33-63
129. K.Kohse-Hoinghaus, P.Oswald, T.A.Cool, T.Kasper, N.Hansen, F.Qi, C.K.Westbrook, and P.R.Westmoreland *Biofuel Combustion: From ethanol to biodiesel*
Angew Chem Int Ed 2010, **49**, 3572-3597
130. A.Dufour et al. Revealing the chemistry of biomass pyrolysis by means of tunable synchrotron photoionisation mass spectrometry *RSC Advances* 2013, **3**, 4786-4792
131. C.A.Taatjes, N.Hansen, D.L.Osborn, K.Kohse-Hoinghaus, T.A.,Cool and P.R.Westmoreland “Imaging” combustion chemistry via multiplexed synchrotron-photoionization mass spectrometry *PCCP* 2008 **10**, 20-34
132. D.Felsmann, K.Moshhammer, J.Kruger, A.Lackner, A.Brockhinke, T.Kasper, T.Bierkandt, E.Akyildiz, N.Hansen, A.Lucassen, P.Oswald, M.Kohler, G.A.Garcia, L.Nahon, P.Hemberger, A Bodi, T.Gerber, and K.Kohse-Hoinghaus Electron ionization, photoionization and photoelectron/photoion coincidence spectroscopy in mass-spectrometric investigations of a low-pressure ethylene/oxygen flame
Proceedings of the Combustion Inst. 2015, **35**, 779-786

133. N.Hansen, T.A.Cool, P.R.Westmoreland and K.Kohse-Hoinghaus Recent contributions of flame-sampling molecular beam mass spectrometry to a fundamental understanding of combustion chemistry Prog. Energy Combust Sci. 2009, **35**, 168-191
134. F.Qi, R.Yang, B.Yang, C.Huang, L.Wei, J.Wang, L.Sheng, and Y.Zhang Isomeric identification of polycyclic aromatic hydrocarbons formed in combustion, with tunable vacuum ultraviolet photoionisation Rev Sci Instrum. 2006, **77**, 084101 (5 pages)
135. D.Kruger, P.Oswald, M.Kohler, P.Hemberger, T.Bierkandt, Y.Karakaya and T.Kasper Hydrogen abstraction ratios: A systematic iPEPICO investigation in laminar flames Combustion and Flame 2018, **191**, 343-352
136. J.A.Kruger, G.A.Garcia, D.Felsmann, K.Moshhammer, A.Lackner, A.Brockhinke, L.Nahon and K.Kohse-Hoinghaus Photoelectron-photoion coincidence spectroscopy of multiplexed detection of intermediate species in a flame PCCP 2014, **16**, 22791-22804
137. P.Hemberger, V.B.Custodis, A.Bodi, T.Gerber, and J.A.van Bokhoven Understanding the mechanism of catalytic fast pyrolysis by unveiling reactive intermediates in heterogeneous catalysis Nature Communications 2017, **8**, Art No 15946, June 29,
138. A.Bodi, P.Hemberger, D.L.Osborn, and B.Sztaray Mass resolved isomer-selective chemical analysis with photoelectron photoion coincidence spectroscopy J.Phys Chem Lett 2013, **4**, 2948-2952
139. D. Felsmann, A.Lucassen, J.Kruger, C.Hemken, L.S.Tran, J.Pieper, G.A.Garcia, A.Brockhinke, L.Nahon, and K.Kohse-Hoinghaus Progress in Fixed-Photon-Energy Time-Efficient Double Imaging Photoelectron/Photoion Coincidence Measurements in Quantitative Flame Analysis Zeitschrift für Physikalische Chemie 2016, **230**, 1067-1097
140. J.Pieper, S.Schmitt, C.Hemken, E.Davies, J.Wullenkord, A.Brockhinke, J.Kruger, G.A.Garcia, L.Nahon, A.Lucassen, W.Eisfeld and K.Kohse-Hoinghaus Isomer Identification in Flames with Double-Imaging Photoelectron/Photoion Coincidence Spectroscopy (i2PEPICO) using Measured and Calculated Reference Photoelectron Spectra Zeitschrift für Physikalische Chemie 2018, **232**, 153-187.
141. X.Tang, G.A.Garcia, and L.Nahon CH_3^+ formation in the dissociation of energy-selected CH_3F^+ studied by double imaging electron-ion coincidences

J.Phys Chem A 2015, **119**, 5942-5950

142. M.Alagia,. E.Bodo, P.Decleva, S.Falcinelli, A.Ponzi, R.Richter and S.Stranges The soft X-ray absorption spectrum of the allyl free radical PCCP 2013, **15**, 1310-1318

143.P.Hemberger, M.Lang, B.Noller, I Fischer, C.Alcaraz, B.K.Cunda de Miranda, G.A.Garcia and H.Soldi-Lose Photoionization of Propargyl and Bromopropargyl Radicals: A Threshold Photoelectron Spectroscopic Study J.Phys Chem A 2011, **115**, 2225-2230

144. S.Willitsch, J.M.Dyke and F.Merckt Rotationally resolved photoelectron spectrum of the lowest singlet electronic state of NH_2^+ and ND_2^+ : photoionization dynamics and rovibrational energy level structure of the $\tilde{a}^1\text{A}_1$ state
Molecular Physics 2004, **102**, 1543-1553

145. S.Willitsch, F.Merckt, M.Kallay and J.Gauss Thermochemical properties of small open-shell systems: experimental and high level *ab initio* results for NH_2 and NH_2^+
Molecular Physics 2006, **104**, 1457-1461

146. L.G.Dodson, J.D.Savee, S.Gozem, L.Shen, A.I.Krylov, C.A.Taatjes, D.L.Osborn, and M.Okumura Vacuum ultraviolet photoionization cross section of the hydroxyl radical
J.Chem Phys 2018, **148**, 184302 (11 pages)

147. O.J.Harper, M.Hassenfratz, J.C.Loison, G.A.Garcia, N.de Oliveira, H.R.Hrodmarsson, S.T.Pratt, S.Boye-Peronne, and B.Gans Quantifying the photoionization cross section of the hydroxyl radical J.Chem Phys Communications 2019 (in press)
doi:10.1021/acs.jpca.8b11809

148. G.Gans, L.A.Vieira Mendes, S.Boye-Peronne, S.Douin, G.Garcia, H.Soldi-Lose, B.K.Cunha de Miranda, C.Alcaraz, N. Carrasco, P.Pernot and D.Gauyacq
Determination of the Absolute Photoionization Cross Section of CH_3 and I Produced from a Pyrolysis Source, by Combined Synchrotron and Vacuum Ultraviolet Laser Studies
J.Phys Chem A 2010, **114**, 3237-3246

149. B.Gans, G.A.Garcia, S.Boye-Peronne, J.C.Loison, S.Douin, F.Gai-Levrel and D.Gauyacq Absolute Photoionization Cross section of the Ethyl Radical in the Range 8.0-11.5 eV: Synchrotron and Vacuum Ultraviolet Laser Measurements
J.Phys Chem A 2011, **115**, 5387-5396

150. H.R.Hrodmarsson, J.C.Loison, U.Jacovella, D.M.P.Holland, S.Boye-Peronne, B.Gans, G.A.Garcia, L.Nahon, and S.T.Pratt
Valence-Shell Photoionization of C₄H₅: The 2-Butyn-1-yl Radical
J.Phys Chem A 2019, **123**, 1521-1528